Universiteit
Leiden
The Netherlands

The JWST early release science program for the direct imaging and spectroscopy of exoplanetary systems

Hinkley, S.; Carter, A.L.; Ray, S.; Skemer, A.; Biller, B.; Choquet, E.; ... ; Ygouf, M.

Citation
Hinkley, S., Carter, A. L., Ray, S., Skemer, A., Biller, B., Choquet, E., … Ygouf, M. (2022). The JWST early release science program for the direct imaging and spectroscopy of exoplanetary systems. *Publications Of The Asp*, *134*(1039). doi:10.1088/1538-3873/ac77bd

Version:	Publisher's Version
License:	Creative Commons CC BY 4.0 license
Downloaded from:	https://hdl.handle.net/1887/3512426

Note: To cite this publication please use the final published version (if applicable).

Publications of the Astronomical Society of the Pacific, 134:095003 (20pp), 2022 September https://doi.org/10.1088/1538-3873/ac77bd
© 2022. The Author(s). Published by IOP Publishing Ltd on behalf of the Astronomical Society of the Pacific (ASP). All rights reserved

OPEN ACCESS

The JWST Early Release Science Program for the Direct Imaging and Spectroscopy of Exoplanetary Systems

Sasha Hinkley[1], Aarynn L. Carter[2], Shrishmoy Ray[1], Andrew Skemer[2], Beth Biller[3], Elodie Choquet[4], Maxwell A. Millar-Blanchaer[5], Stephanie Sallum[6], Brittany Miles[2], Niall Whiteford[7], Polychronis Patapis[8], Marshall Perrin[9], Laurent Pueyo[9], Glenn Schneider[10], Karl Stapelfeldt[11], Jason Wang[12,13], Kimberly Ward-Duong[9,14], Brendan P. Bowler[15], Anthony Boccaletti[16], Julien H. Girard[9], Dean Hines[9], Paul Kalas[17], Jens Kammerer[9], Pierre Kervella[16], Jarron Leisenring[10], Eric Pantin[18], Yifan Zhou[15], Michael Meyer[19], Michael C. Liu[20], Mickael Bonnefoy[21], Thayne Currie[22], Michael McElwain[23], Stanimir Metchev[24], Mark Wyatt[25], Olivier Absil[26], Jea Adams[27], Travis Barman[28], Isabelle Baraffe[1,29], Mariangela Bonavita[30], Mark Booth[31], Marta Bryan[17], Gael Chauvin[21], Christine Chen[9], Camilla Danielski[32,33], Matthew De Furio[19], Samuel M. Factor[15], Michael P. Fitzgerald[34], Jonathan J. Fortney[2], Carol Grady[35], Alexandra Greenbaum[36], Thomas Henning[37], Kielan K. W. Hoch[9], Markus Janson[38], Grant Kennedy[39], Matthew Kenworthy[40], Adam Kraus[15], Masayuki Kuzuhara[41,42], Pierre-Olivier Lagage[33], Anne-Marie Lagrange[21], Ralf Launhardt[37], Cecilia Lazzoni[1,43], James Lloyd[44], Sebastian Marino[25,45], Mark Marley[28], Raquel Martinez[6], Christian Marois[46,47], Brenda Matthews[46,47], Elisabeth C. Matthews[48], Dimitri Mawet[11,12], Johan Mazoyer[16], Mark Phillips[20], Simon Petrus[21,49], Sascha P. Quanz[8], Andreas Quirrenbach[50], Julien Rameau[21], Isabel Rebollido[9], Emily Rickman[51], Matthias Samland[37], B. Sargent[9,52], Joshua E. Schlieder[53], Anand Sivaramakrishnan[9], Jordan M. Stone[54], Motohide Tamura[41,42,55], Pascal Tremblin[56], Taichi Uyama[57,58], Malavika Vasist[26], Arthur Vigan[4], Kevin Wagner[10,59], and Marie Ygouf[11]

[1] University of Exeter, Astrophysics Group, Physics Building, Stocker Road, Exeter, EX4 4QL, UK
[2] Department of Astronomy & Astrophysics, University of California, Santa Cruz, CA 95064, USA
[3] SUPA, Institute for Astronomy, The University of Edinburgh, Royal Observatory, Blackford Hill, Edinburgh, EH9 3HJ, UK
[4] Aix Marseille Univ., CNRS, CNES, LAM, Marseille, France
[5] Department of Physics, University of California, Santa Barbara, Santa Barbara, CA, USA
[6] Department of Physics and Astronomy, University of California, Irvine, Irvine, CA, USA
[7] Department of Astrophysics, American Museum of Natural History, Central Park West at 79th Street, NY 10024, USA
[8] Institute for Particle Physics & Astrophysics, ETH Zurich, 8092 Zurich, Switzerland
[9] Space Telescope Science Institute, 3700 San Martin Drive, Baltimore, MD 21218, USA
[10] Steward Observatory, University of Arizona, 933 N. Cherry Ave, Tucson, AZ 85721-0065 USA
[11] Jet Propulsion Laboratory, California Institute of Technology, M/S 321-100, 4800 Oak Grove Drive, Pasadena, CA 91109, USA
[12] Department of Astronomy, California Institute of Technology, Pasadena, CA 91125, USA
[13] Center for Interdisciplinary Exploration and Research in Astrophysics (CIERA) and Department of Physics and Astronomy, Northwestern University, Evanston, IL 60208, USA
[14] Department of Astronomy, Smith College, Northampton MA 01063, USA
[15] Department of Astronomy, The University of Texas at Austin, 2515 Speedway Boulevard Stop C1400, Austin, TX 78712, USA
[16] LESIA, Observatoire de Paris, Université PSL, CNRS, Sorbonne Université, Université Paris Cité, 5 place Jules Janssen, F-92195 Meudon, France
[17] Department of Astronomy, University of California at Berkeley, CA 94720, USA
[18] IRFU/DAp Département D'Astrophysique CE Saclay, Gif-sur-Yvette, France
[19] Department of Astronomy, University of Michigan, Ann Arbor, MI 48109, USA
[20] Institute of Astronomy, University of Hawaii, 2860 Woodlawn Drive, Honolulu, HI 96822, USA
[21] Université Grenoble Alpes/CNRS, Institut de Planétologie et dAstrophysique de Grenoble, F-38000 Grenoble, France
[22] NASA-Ames Research Center, Moffett Field, California, USA
[23] NASA-Goddard Space Flight Center, Greenbelt, MD, USA
[24] Department of Physics and Astronomy, Centre for Planetary Science and Exploration, The University of Western Ontario, London, ON N6A 3K7, Canada
[25] Institute of Astronomy, University of Cambridge, Madingley Road, Cambridge CB3 0HA, UK
[26] Space Sciences, Technologies, and Astrophysics Research (STAR) Institute, University of Liège, B-4000 Liège Belgium
[27] Center for Astrophysics | Harvard & Smithsonian, 60 Garden St, Cambridge, MA 02138, USA
[28] Lunar & Planetary Laboratory, University of Arizona, Tucson, AZ 85721, USA
[29] École Normale Supérieure, Lyon, CRAL (UMR CNRS 5574), Université de Lyon, France
[30] School of Physical Sciences, The Open University, Walton Hall, Milton Keynes, MK7 6AA
[31] Astrophysikalisches Institut und Universitätssternwarte, Friedrich-Schiller-Universität Jena, Schillergässchen 2-3, D-07745 Jena, Germany
[32] Instituto de Astrofísica de Andalucía, CSIC, Glorieta de la Astronomía s/n , E-18008, Granada, Spain
[33] AIM, CEA, CNRS, Universitè Paris-Saclay, Universitè Paris Diderot, Sorbonne Paris Citè, F-91191 Gif-sur-Yvette, France
[34] Department of Physics & Astronomy, University of California, Los Angeles, CA 90095, USA
[35] Eureka Scientific, 2452 Delmer St., Suite 100, Oakland CA 96402-3017, USA
[36] IPAC, Mail Code 100-22, Caltech, 1200 E. California Blvd., Pasadena, CA 91125, USA
[37] Max-Planck-Institut für Astronomie, Königstuhl 17, D-69117 Heidelberg, Germany
[38] Department of Astronomy, Stockholm University, SE-10691, Stockholm, Sweden
[39] Department of Physics, University of Warwick, Coventry CV4 7AL, UK
[40] Leiden Observatory, Leiden University, Postbus 9513, 2300 RA Leiden, The Netherlands

[41] Astrobiology Center, 2-21-1, Osawa, Mitaka, Tokyo, 181-8588, Japan
[42] National Astronomical Observatory of Japan, 2-21-1 Osawa, Mitaka, Tokyo 181-8588, Japan
[43] INAF–Osservatorio Astronomico di Padova, Vicolo dell'Osservatorio 5, I-35122, Padova, Italy
[44] Department of Astronomy, Cornell University, Ithaca NY, USA
[45] Jesus College, University of Cambridge, Jesus Lane, Cambridge CB5 8BL, UK
[46] Herzberg Astronomy & Astrophysics Research Centre, National Research Council of Canada, 5071 West Saanich Road, Victoria, BC V9E 2E7, Canada
[47] Department of Physics & Astronomy, University of Victoria, 3800 Finnerty Road, Victoria, BC V8P 5C2, Canada
[48] Observatoire Astronomique de líUniversité de Genève, 51 Ch. Pegasi, 1290 Versoix, Switzerland
[49] Nícleo Milenio Formaciín Planetaria—NPF, Universidad de Valparaíso, Av. Gran Bretaía 1111, Valparaíso, Chile
[50] Landessternwarte, Zentrum für Astronomie der Universität Heidelberg, Königstuhl 12, D-69117 Heidelberg, Germany
[51] European Space Agency (ESA), ESA Office, Space Telescope Science Institute, 3700 San Martin Drive, Baltimore, MD 21218, USA
[52] Center for Astrophysical Sciences, The William H. Miller III Department of Physics and Astronomy, Johns Hopkins University, Baltimore, MD 21218, USA
[53] Exoplanets & Stellar Astrophysics Laboratory, NASA Goddard Space Flight Center, Greenbelt, MD, USA
[54] US Naval Research Laboratory, Remote Sensing Division, 4555 Overlook Ave SW, Washington, DC 20375, USA
[55] Department of Astronomy, The University of Tokyo, 7-3-1, Hongo, Bunkyo-ku, Tokyo 113-0033, Japan
[56] Maison de la Simulation, CEA, CNRS, Univ. Paris-Sud, UVSQ, Universitè Paris-Saclay, F-91191 Gif-sur-Yvette, France
[57] Infrared Processing and Analysis Center, California Institute of Technology, 1200 E. California Blvd., Pasadena, CA 91125, USA
[58] NASA Exoplanet Science Institute, Pasadena, CA 91125, USA
[59] NASA Hubble Fellowship Program—Sagan Fellow
Received 2022 March 24; accepted 2022 June 7; published 2022 September 21

Abstract

The *direct* characterization of exoplanetary systems with high-contrast imaging is among the highest priorities for the broader exoplanet community. As large space missions will be necessary for detecting and characterizing exo-Earth twins, developing the techniques and technology for direct imaging of exoplanets is a driving focus for the community. For the first time, JWST will directly observe extrasolar planets at mid-infrared wavelengths beyond 5 μm, deliver detailed spectroscopy revealing much more precise chemical abundances and atmospheric conditions, and provide sensitivity to analogs of our solar system ice-giant planets at wide orbital separations, an entirely new class of exoplanet. However, in order to maximize the scientific output over the lifetime of the mission, an exquisite understanding of the instrumental performance of JWST is needed as early in the mission as possible. In this paper, we describe our 55 hr Early Release Science Program that will utilize all four JWST instruments to extend the characterization of planetary-mass companions to $\sim$15 μm as well as image a circumstellar disk in the mid-infrared with unprecedented sensitivity. Our program will also assess the performance of the observatory in the key modes expected to be commonly used for exoplanet direct imaging and spectroscopy, optimize data calibration and processing, and generate representative data sets that will enable a broad user base to effectively plan for general observing programs in future Cycles.

Unified Astronomy Thesaurus concepts: Coronagraphic imaging (313); Direct imaging (387); Exoplanet detection methods (489); Space telescopes (1547); Exoplanet atmospheres (487)

1. Introduction

In the relatively short span of a quarter century, astronomers have transitioned from speculating about the prevalence of exoplanetary systems to discovering thousands, and it is now clear that most stars host planetary systems (e.g., Cassan et al. 2012; Dressing & Charbonneau 2013). The vast majority of these, however, have been identified only indirectly via the transit and radial velocity detection methods, and lie at close orbital separations from their host stars.

As the indirect transit and Doppler detection methods are inherently much less sensitive to wide-separation planets with long orbital periods, the direct imaging technique (e.g., Bowler 2016) will be the only approach to fully define the outermost architectures of planetary systems ($\sim$10 to hundreds of au), and provide a more complete understanding of the true frequency of planetary-mass companions to nearby stars (e.g., Nielsen et al. 2019; Vigan et al. 2021). In the last decade, imaging observations mostly at wavelengths of $\lesssim$2 μm have produced numerous scattered light images of circumstellar disks (Esposito et al. 2020), and directly revealed $\sim$10–20, young ($\lesssim$50 Myr), massive ($\gtrsim$1 M_{Jup}) planets (e.g., Marois et al. 2008; Lagrange et al. 2010; Rameau et al. 2013; Chauvin et al. 2017; Macintosh et al. 2015; Bohn et al. 2020; Janson et al. 2021). Direct Imaging is also the only technique that will be capable of characterizing exoplanets at orbital radii $\gtrsim$0.5 au, as transit transmission spectroscopy (e.g., Sing et al. 2016) requires multiple transits to achieve a strong signal for Earth-mass planets on Earth-like orbits around Sun-like stars (Morley et al. 2017) resulting in prohibitively long time baselines. It is

Original content from this work may be used under the terms of the Creative Commons Attribution 3.0 licence. Any further distribution of this work must maintain attribution to the author(s) and the title of the work, journal citation and DOI.

also the only technique projected to provide the in-depth characterization of such exo-Earths (e.g., The LUVOIR Team 2019; Quanz et al. 2021).

By spatially separating the light of the host star and the extremely faint planet, the direct imaging technique is also naturally suited to direct spectroscopy of planets themselves, allowing detailed characterization (e.g., Bowler et al. 2010; Macintosh et al. 2015; De Rosa et al. 2016; Chauvin et al. 2017; Currie et al. 2018). In addition to providing information on atmospheric properties and compositions (e.g., Hinkley et al. 2015a; Kammerer et al. 2021), the direct imaging technique can provide powerful estimations of fundamental parameters, e.g., luminosity, effective temperature, and orbital properties (Gravity Collaboration et al. 2019). The characterization power of the direct imaging method becomes even more pronounced when combined with other exoplanet detection techniques, such as precise radial velocity monitoring or astrometry (e.g., Nowak et al. 2020; Lagrange et al. 2020; Wang et al. 2021a; Lacour et al. 2021), to more fully constrain parameters (e.g., planet mass) that are difficult to ascertain with one technique alone.

Going forward, direct imaging will ultimately provide direct, high-resolution ($R \sim 30{,}000$–$100{,}000$) spectra of exoplanet atmospheres (e.g., Snellen et al. 2015; Mawet et al. 2018; Otten et al. 2021; Wang et al. 2021b). Obtaining photons directly from the atmosphere of the exoplanet itself will allow us to apply to exoplanetary atmospheres all of the spectroscopic techniques that have been applied to stars and brown dwarfs over the last century. Indeed, all of the detailed information that can be retrieved using high-resolution spectroscopy of stars and brown dwarfs (e.g., chemical abundances, compositions, thermodynamic conditions, Doppler tomography) will also be directly obtained for exoplanetary atmospheres, allowing much more precise interpretation of the spectra (Konopacky et al. 2013; Barman et al. 2015).

At the same time, the direct imaging technique has been especially prolific at imaging both very young primordial (protoplanetary) disks as well as dusty circumstellar debris disks. Direct images of these disk structures uniquely allow the study of the dynamical interactions between circumstellar disks, and the planets that are dynamically sculpting them (Choquet et al. 2016; Matthews et al. 2017; Avenhaus et al. 2018; Esposito et al. 2020). Upcoming space-based missions, the advent of the 30–40 m telescopes, as well as updates to existing ground-based high-contrast imaging platforms (e.g., MagAOX, GPI 2.0, SPHERE+, SCExAO; Males et al. 2018; Chilcote et al. 2020) will vastly improve exoplanet direct detection capabilities. Consequently, the development of the direct imaging technique will be a major priority for the broader exoplanet community going forward, and is a key mode for current and future space missions including JWST (Gardner et al. 2006).

1.1. JWST

JWST will be transformative for characterizing exoplanet atmospheres at mid-infrared and longer wavelengths (3–28 μm). In addition to a handful of spectra of free-floating brown dwarfs from The Spitzer Space Telescope and *Akari* missions (Cushing et al. 2006; Sorahana & Yamamura 2012), direct images of exoplanets from 3 to 5 μm exist (e.g., Galicher et al. 2011; Skemer et al. 2014, 2016), but the extremely high telluric background has imposed a strong sensitivity barrier. Transit transmission spectroscopy of transiting "Hot Jupiter" exoplanets using the Spitzer Space Telescope exist (e.g., Grillmair et al. 2007, 2008), but this class of planet has very different properties than young planets studied via direct imaging, or even solar system giant planets. Even further, despite some tantalizing early detections (e.g., Wagner et al. 2021), exoplanets have never been directly observed at wavelengths $\gtrsim$5 μm.

To date, much of the instrumentation dedicated to the purpose of high-contrast imaging (Hinkley et al. 2011b; Macintosh et al. 2018; Beuzit et al. 2019) has operated at wavelengths $\lesssim$3 μm. However, in addition to observing planets closer to the peak of their thermal emission, obtaining exoplanet photometry and spectroscopy at 3–5 μm is a key probe of atmospheric compositions, and dramatically improves differentiation between equilibrium and disequilibrium atmospheric chemistry (Skemer et al. 2012; Phillips et al. 2020; Miles et al. 2020). As well as clear markers of composition, many of the key atmospheric processes that shape the spectra of planetary-mass companions, e.g., vertical atmospheric mixing (Hubeny & Burrows 2007; Barman et al. 2011), cloud physics, and the presence of patchy cloud structures (Currie et al. 2011) have signatures at the wavelengths observable by JWST. These sets of constraints cannot be entirely accessed through observations at 1–2 μm alone. Incorporating data at long wavelengths can dramatically help to break the persistent degeneracies (see e.g., Chabrier et al. 2007) in the interpretation of exoplanet spectra that might be in fact driven by enhanced elemental abundances, or various physical processes such as vertical atmospheric mixing (Konopacky et al. 2013). While JWST will not have the angular resolution, nor the inner working angles, of 8–10 m ground-based telescopes operating in the near-infrared (Perrin et al. 2018), the extremely precise flux measurements afforded by the stability and low thermal background at the second Lagrange point will allow the differentiation of dominant exoplanet atmospheric chemistries, as well as derive circumstellar disk compositions.

The long-wavelength coverage offered by JWST will provide abundances of the expected molecules in exoplanet atmospheres (CH_4, CO, CO_2, H_2O and NH_3), using multiple features and a broad wavelength range to distinguish between clouds and molecular absorption. Calculating abundances for the major oxygen and carbon-bearing species will provide measurements of an object's C/O ratio. Whether or not the

C/O ratio of a companion matches that of its star may provide clues regarding the companion formation mechanism, and may help to distinguish zones of formation within the protoplanetary disk (Öberg et al. 2011; Cridland et al. 2016, 2019; Mollière et al. 2022). However, the utility and ease of a single metric such as the C/O ratio to capture the complex physics (e.g., Fortney et al. 2013; Cridland et al. 2016; Madhusudhan et al. 2017) inherent in the planet formation process has been debated. For example, some works (e.g., Mordasini et al. 2016) have demonstrated how limitations in our understanding of disk chemistry, the planet formation process and migration can limit the utility of this metric.

Differences in the near-infrared Spectral Energy Distributions (SEDs) of exoplanets and field brown dwarfs (Chauvin et al. 2004; Marois et al. 2008) suggest that their atmospheres are not the same, perhaps due to differences in surface gravity (Marley et al. 2012), stellar insolation (Zahnle et al. 2016), or cloud features. This difference is readily apparent in color–magnitude diagrams, where planetary-mass objects tend to be much redder than the field brown dwarf population (Faherty et al. 2016; Liu et al. 2016). Silicate and iron clouds are typically used to explain the colors of red (L-type) brown dwarfs, but the colors can also be explained by thermochemical instabilities (Tremblin et al. 2015, 2016) or the viewing angle (Vos et al. 2017). Although there have been tentative detections of silicates through an 8-12 μm absorption feature in field brown dwarfs with Spitzer (Cushing et al. 2006; Looper et al. 2008), extremely red exoplanets might have stronger features that point toward the cloud hypothesis. Moving forward, it will be essential to gather empirical constraints on these SEDs in order to effectively model the sensitivity of JWST to these substellar objects in future surveys.

JWST utilizes four science instruments operating in the infrared, with three of these operating at wavelengths shorter than 5 μm. NIRCam (Rieke et al. 2005; Beichman et al. 2012) and NIRSpec (Bagnasco et al. 2007; Jakobsen et al. 2022) are the primary near-infrared imager and spectrograph, respectively, but only NIRCam and MIRI offer a coronagraphic mode. NIRCam offers a series of coronagraphic occulting masks (Green et al. 2005; Krist et al. 2007) and preflight estimates of the coronagraphic performance suggest that contrasts of $\sim 10^{-4}$–10^{-5} within $\sim 1''$ will be achieved. NIRSpec will have numerous capabilities for spectroscopically characterizing the atmospheres of extrasolar planets (e.g., Birkmann et al. 2022), including obtaining direct spectroscopy for widely separated companions. NIRISS (Doyon et al. 2012) is equipped with an Aperture Masking Interferometer mode ("AMI," Sivaramakrishnan et al. 2012; Artigau et al. 2014; Soulain et al. 2020) with the goal of obtaining moderate contrast (10^{-3}–10^{-4}) at separations comparable to (and within) the JWST diffraction limit of 130-150 mas at $\sim$4–5 μm. MIRI (Rieke et al. 2015; Wright et al. 2015) is the only instrument capable of observations at wavelengths longer than 5 μm, and is equipped with four-quadrant phase mask (FQPM) coronagraphs (Rouan et al. 2000; Baudoz et al. 2006) operating at 10.65, 11.60, and 15.5 μm, as well as a classical Lyot coronagraph operating at 23 μm (Boccaletti et al. 2005; Cavarroc et al. 2008; Boccaletti et al. 2015). In addition to offering very good contrast performance at small inner working angles of $\sim \lambda/D$ at wavelengths of 10–16 μm, the 4QPM coronagraph design was chosen during the MIRI design phase as it was one of the few coronagraphs that had been validated both in laboratory testing as well as on sky. Below we describe some of the potentially transformative science that will be done with JWST coronagraphy for identifying wide-separation giant planets, as well as characterizing circumstellar debris disks.

1.2. A New Class of Planets: Wide-Separation Saturn & Neptune Analogues

The exquisite thermal infrared sensitivity afforded by JWST means that it will be possible for the first time to directly image sub-Jupiter mass planets, an entirely new class of directly imaged planet (Beichman et al. 2010; Carter et al. 2021b). Previous studies (e.g., Janson et al. 2015) have demonstrated the gain in sensitivity when using space-based imaging at infrared wavelengths, similar to those to be used with the JWST NIRCam instrument. In the background-limited regime within the field of view, JWST will have 50 times the sensitivity of the Gemini Planet Imager (Macintosh et al. 2015) operating at 2 μm, and 500 times the sensitivity of the Keck/NIRC2 instrument at 4 μm (Perrin et al. 2018). Analogues to our own solar system ice-giant planets should have very cold temperatures, and thus the peak wavelength of their emission will be shifted out of the near- and mid-infrared (1 to $\sim$5 μm) into to the thermal infrared ($\gtrsim$10 μm). The very high telluric background from the ground imposes a stark sensitivity limit, even with new technologies (e.g., adaptive secondary mirrors). Thus, in addition to potentially directly detecting a handful of planets detected by the radial velocity technique (e.g., Brande et al. 2020), the superior thermal infrared sensitivity of JWST will allow imaging for the first time of wide, young Saturn analogues in many cases down to masses of 0.2 $M_{\rm Jup}$. In the most favorable cases, JWST will be capable of directly imaging wide young Neptune analogues (Beichman et al. 2010; Schlieder et al. 2016; Carter et al. 2021b).

Early results from direct imaging surveys (e.g., Nielsen et al. 2019; Wagner et al. 2019; Vigan et al. 2021) suggest that an abundant population of lower mass planetary companions exists at wide orbital separations (tens to hundreds of AU). Extrapolating the mass distribution power laws derived by the GPI campaign (Nielsen et al. 2019) indicates several 0.1–1.0 $M_{\rm Jup}$ planets per star reside at separations of 10–100 au when considering the broadest range of host star masses (0.2–5 $M_{\odot}$). Along the same lines, Fernandes et al. (2019) predict a factor of $\sim$2–4 increase in occurrence rate between 10–100 au for

0.1–13 $M_{\rm Jup}$ planets compared to 1–13 $M_{\rm Jup}$ planets. Recent statistical arguments from microlensing efforts (e.g., Poleski et al. 2020) are consistent with this, suggesting ∼1.5 ice-giant planets ($\lesssim$1 $M_{\rm Jup}$) per star reside between 5–15 au. The sensitivity of JWST to such a wide range of masses (several $M_{\rm Jup}$ down to $\lesssim$1 $M_{\rm Jup}$) has the potential to associate sub-populations of planets to various planet formation mechanisms. For example, it is expected that the gravitational instability model (Kratter et al. 2010; Forgan & Rice 2013) will preferentially form planets with masses $\gtrsim$3 $M_{\rm Jup}$, while lower mass planets on such wide orbits are challenging to form via this model, and instead suggest a mechanism more akin to a model based on accretion of solids in a protoplanetary disk (e.g., Pollack et al. 1996). Therefore, measuring the mass and separation functions of wide-orbit, low-mass companions is also a powerful constraint on the specifics of a formation mechanism based on core accretion.

1.3. Studies of Circumstellar Disks with JWST

Exoplanets and circumstellar debris disks go hand-in-hand: the gravitational influence of giant planets in these systems shapes the belts of debris, generated by colliding remnant planetesimals (Wyatt 2008; Hughes et al. 2018), can exist in stable orbits around a star, and sculpts the dust distribution through scattering, secular interactions and resonances (Chiang et al. 2009; Wyatt 2003; Morrison & Malhotra 2015). Indeed, the structure of debris disks reveal dynamical relations between planets and their circumstellar environment, and any evaluation of JWST's ability to characterize planetary systems must also include its ability to characterize diffuse, extended emission from circumstellar debris disks.

With nearly an order of magnitude greater angular resolution than Spitzer, JWST will allow resolved imaging of asteroid belts in other systems for the first time. The very large, contiguous fields-of-view of NIRCam and MIRI, coupled with their high sensitivity, will be critically important for studies of debris disks, providing access to regions at high-contrast beyond the control zones of ground-based Adaptive Optics systems (e.g., ∼0.″5–1.″0 , Matthews et al. 2018; Hinkley et al. 2021). H_2O ice features are strong in Saturn's rings and Kuiper Belt objects (e.g., Filacchione et al. 2014) and are expected in debris disks, but sufficiently sensitive observations have been impossible from the ground. In addition to constraining the dust scattering properties, NIRCam observations of debris disks may potentially directly detect the planets responsible for driving the ring structures, or provide very sensitive upper limits on their presence. Due to very high CO_2 opacity in Earth's atmosphere, debris disks have *never* been imaged specifically at 15 μm—on the steeply rising Wien side of the disk thermal emission. Spatially resolved 15 μm debris disk observations will constrain the disk radial temperature profiles (and thus dust grain sizes), and disentangle the unresolved excess emission close to the star from the extended emission in the outer, bright debris structures. JWST is well poised to address these issues, but the best observing practices need to be established quickly.

In this paper, we describe our upcoming 55 hr Early Release Science (ERS) Program dedicated to the direct imaging and spectroscopy of extrasolar planetary systems. In Section 2 we provide our rationale for an ERS program dedicated to this task, and in Section 3 we provide a detailed overview of the observational strategy of our program. In Section 4 we describe our plans for rapid data processing as well as the Science Enabling Products ("SEPs") our team will deliver shortly after the program is executed, and in Section 5 we provide a summary and conclude.

2. Rationale for a JWST Early Release Science Program

JWST will be a transformative observatory for directly characterizing both exoplanets and their circumstellar environments. It will enable very sensitive, high-fidelity imaging and spectrophotometry of exoplanetary systems in the near/mid-infrared with NIRCam, NIRSpec, and NIRISS, and with MIRI at wavelengths $\gtrsim$5 μm for the first time. However, imaging young extrasolar giant planets and disks at very small angular separations from a host star is an extreme technical challenge: at young ages (∼1–100 Myr) even the most massive planets are typically $\sim 10^3$–10^6 times fainter than the host star, and buried in the halo of the instrumental Point-Spread Function (PSF). At such a high level of contrast, an exquisite understanding is required of the instrument response, PSF stability, and PSF subtraction techniques during post-processing. To this end, successfully obtaining images of planets and circumstellar disks requires the correct choice of observation mode and extremely careful post-processing.

As described in Perrin et al. (2018), the last ∼25 yr of highly successful coronagraphy and high-contrast imaging with The Hubble Space Telescope (HST) provides a very useful set of lessons for the best path forward with JWST. One clear lesson from the HST legacy is that, particularly for non-optimal coronagraphs (e.g., those on board HST or even JWST), more of the contrast gains come from state-of-the-art starlight suppression work in the image post-processing stage than from suppression at the hardware level (Pueyo 2016; Choquet et al. 2016; Perrin et al. 2018; Zhou et al. 2021; Sanghi et al. 2022). Indeed, exquisite calibration of the PSF is key, and typically this is carried out by using some variation of the Angular Differential Imaging technique ("ADI," Marois et al. 2006) to utilize the rotation of the observatory to disentangle bona fide astrophysical sources (e.g., planets) from the residual scattered starlight. For each individual science image, the task is to use other images in the sequence that do not contain a signal of the planet to construct an optimized, synthetic model of the PSF, typically using least-squares ("LS," Lafrenière et al. 2007), or

principal component analysis methods ("PCA," Soummer et al. 2012; Amara & Quanz 2012) to generate synthetic PSF calibrations that are optimally matched to each science exposure. However, JWST will typically only achieve ~5° of rotation when the spacecraft is rolled slightly, meaning that the sensitivity of JWST will be limited at close separations from the star. However, it has now been well demonstrated, especially for space-based imaging such as HST/NICMOS (Soummer et al. 2011) with PSF morphologies that are highly stable in time, that using a vast suite of reference PSF images from other epochs/targets can alleviate this problem. Indeed, over its lifetime, JWST will provide such an extensive library of images, but not necessarily in the early phases of the mission.

Coronagraphic imaging with HST required several cycles to optimize the observing strategy and PSF calibration methods, and the methods are still being refined (e.g., Schneider et al. 2017; Zhou et al. 2021). Further, applying techniques originally developed for the ground to HST archival coronagraphic data (Lafrenière et al. 2009; Soummer et al. 2011) has revealed vastly improved sensitivity to imaging planets and disks including numerous new discoveries from archival data (Soummer et al. 2014; Choquet et al. 2016; Sanghi et al. 2022). Similar methods and algorithms may be applicable to JWST images, provided the correct observing strategy and data processing methods are identified as early as possible, and used consistently going forward. Although the JWST instruments have been characterized during instrument testing, neither the in-flight performance of each instrument, nor the optimal strategy for obtaining data in flight, or even the optimal ways to post-process the data are well understood.

The finite lifetime of the JWST mission means that it is essential to correctly optimize and implement the observing strategies as early as possible for gaining spectrophotometry and images of exoplanets and circumstellar disks. In anticipation of this need, in 2009 the Space Telescope Science Institute (STScI) appointed the JWST Advisory Committee (JSTAC) to provide a recommendation on how best to maximize the scientific return of JWST. One of the recommendations was to create a clear pathway "to enable the community to understand the performance of JWST prior to the submission of the first post-launch Cycle 2 proposals that will be submitted just months after the end of commissioning".[60] In response, the STScI Director created the JWST Early Release Science (ERS) programs, comprised of ~500 hours of Director's Discretionary Time (DDT). This program was to be characterized by open community access to substantial, representative data sets, in key instrument modes. Along with the SEPs described in Section 4, this effort will support the broader community in the preparation of future JWST proposals, and engage a broad cross-section of the community to familiarize themselves with JWST data and its scientific capabilities.[61]

From 2016-2017 numerous members of the community engaged in research related to the direct imaging and spectroscopy of exoplanets and circumstellar disks self-organized to formulate a program designed to address the key questions about JWST performance that will inform future proposal cycles. A total of 106 proposals were submitted, and 13 proposals were ultimately selected spanning a range of science disciplines including extrasolar planets, solar system, stellar populations and stellar physics, Galaxies and intergalactic medium, and host galaxies to massive black holes.

3. Overview of ERS Program 1386

Our Program "High-Contrast Imaging of Exoplanets and Exoplanetary Systems with JWST" (Program 1386) was awarded 55 hours of DDT to utilize all four JWST instruments, and assess the performance of the observatory in representative modes that are highly applicable to our community going forward. In addition, our team has been tasked to: (1) optimize data calibration and analysis methods; (2) make clear recommendations to our community about the best practices for JWST observing; and (3) generate a set of SEPs, tools that will be essential for the broader community to plan for Cycle 2 proposals (Section 4). The ultimate outcome of this program will be to rapidly establish the optimal strategies for imaging and spectroscopy of exoplanetary systems going forward, and provide the community with a set of tools to help prepare the strongest proposals for Cycle 2 and beyond.

At the same time, our program will showcase the transformative science expected from JWST related to the direct characterization of planetary systems such as highly sensitive coronagraphy, direct spectroscopy into the thermal infrared, and interferometry. Table 1 provides an overview of the targets we will observe and their basic properties. The exoplanet HIP 65426b (Chauvin et al. 2017) and substellar object VHS J125601.92-125723.9b (Gauza et al. 2015; Miles et al. 2018, hereafter "VHS 1256b") are both young companions to their host stars at wide orbital separations, and HD 141569A, is a young (5 ± 3 Myr) circumstellar disk (Clampin et al. 2003) still potentially in the phase of forming a planetary system.

Our program will carry out: 1) coronagraphic imaging of HIP 65426b and 2) HD 141569A at wavelengths extending to 15.5 μm; 3) spectroscopy of VHS 1256b at resolution R ~1500–3000 out to 28 μm; and 4) aperture masking interferometry of a bright star (HIP 65426) at 3.8 μm. Table 2 lists these four primary science tasks and the instruments they will employ, the primary targets for each of these tasks, as well as the objects selected for calibration. Table 2 also lists the wavelength coverage and spectral resolution, as well as details of the chosen

[60] The full description of the recommendations of the JSTAC can be found at: http://www.stsci.edu/jwst/about/history/jwst-advisory-committee-jstac.

[61] More information on the ERS programs can be found at: http://www.stsci.edu/jwst/science-planning/calls-for-proposals-and-policy.

Table 1
A Table Showing the Primary Science Targets to be Observed within this ERS Program

Target	Host Star SpT	Distance (pc)	Age (Myr)	Angular Separation (″)	Mass (M_{Jup})	References
HIP 65426b	A2V	109.2 ± 0.8	14 ± 4	0.83	6–12	Chauvin et al. (2017); Cheetham et al. (2019)
VHS 1256b	M7.5 ± 0.5	$22.2^{+1.1}_{-1.2}$	150–300	8.06 ± 0.03	19 ± 5	Gauza et al. (2015); Dupuy et al. (2020)
HD 141569A	A2	110.6 ± 0.5	5 ± 3	⋯	⋯	Weinberger et al. (2000); Clampin et al. (2003)

Table 2
A Table Showing the Observing Configuration for Each of the Major Tasks in Our Program: Coronagraphy of an Exoplanet and a Circumstellar Disk, Spectroscopy of a Planetary Mass Companion, and Aperture Masking Interferometry

Task (Instruments)	***Targets*** (t_{sci}, t_{obs})	λ Coverage, $\lambda/\Delta\lambda$	***Mode: Filters/Gratings***	t_{sci} (hr)	t_{obs} (hr)
Exoplanet Coronagraphy (NIRCam, MIRI)	Primary: HIP 65426b (5.0, 10.4) Calibrator: HIP 68245 (2.9, 6.0)	2-15 μm	NIRCam MASK335R: F250M, F300M, F410M, F356W, F444W MIRI FQPM: F1140C, F1550C	7.9	16.4
Disk Coronagraphy (NIRCam, MIRI)	Primary: HD 141569A (8.1, 14.2) Calibrator: HD 140986 (5.4, 9.6)	3–15 μm	NIRCam MASK335R: F300M, F360M MIRI FQPM: F1065C, F1140C, F1550C	13.5	23.8
Spectroscopy of a Planetary Mass Companion (NIRSpec, MIRI)	VHS 1256b	1–28 μm, R ∼ 1500–3000	NIRSpec IFS: G140H, G235H, G395H MIRI MRS: All channels	2.7	6.3
Aperture Masking Interferometry (NIRISS)	Primary: HIP 65426 (3.0, 4.7) Calibrator: HD 115842 (0.6, 1.8) Calibrator: HD 116084 (1.0, 2.3)	3.8 μm	F380M	4.6	8.8
				Total: 28.7	***Total: 55.3***

Note. In addition to the instruments used, targets to be observed (both primary and calibration targets), wavelengths/resolution employed, and observing modes, the table also shows in parentheses the partitions of time dedicated purely to science observations (denoted "t_{sci}"), and the time charged to the observatory ("t_{obs}"), which includes observatory overheads. Our program was also awarded an additional ∼12 hrs to collect background observations using MIRI, bringing our true time allocation to ∼68 hrs. These observations were needed to calibrate some stray light effects discovered during MIRI commissioning. However, since such a time commitment is not expected to be typical for future observing programs, we have chosen not to list it in this table.

observing mode, e.g., the NIRCam "MASK335R" or MIRI FQPM coronagraphy, NIRSpec Integral Field Spectrograph (IFS) or the MIRI Medium Resolution Spectrograph (MRS). Table 2 also lists the pure "science time" (denoted "t_{sci}") dedicated to each of these three tasks, as well as the overall time charged to the observatory (denoted "t_{obs}") reflecting spacecraft, observatory, and instrument overheads. In total, our program will utilize 55.3 hr of observing time, with 28.7 of these hours dedicated to pure science observations. A majority of this time will be dedicated to coronagraphic observations of HIP 65426b and HD 141569A (∼40 hr observatory time, "21 hr of science). Below we describe each of these components of the program in greater detail.

3.1. Coronagraphy of an Extrasolar Planet

HIP 65426b is a 6–12 M_{Jup} planetary-mass companion (Chauvin et al. 2017) with a wide projected orbital separation of 92 au, and a young age (14 ± 4 Myr) based on its host star's high probability of membership to the Lower Centaurus Crux association (de Zeeuw et al. 1999; Rizzuto et al. 2011). This was the first major discovery by the SPHERE "SHINE" GTO survey (Desidera et al. 2021; Langlois et al. 2021; Vigan et al. 2021). Initial photometric measurements from 1 to 5 μm (Cheetham et al. 2019; Stolker et al. 2020) and medium resolution spectroscopy (Petrus et al. 2021) of this object are consistent with a dusty, low surface gravity atmosphere with mid/late-L spectral type. The angular separation of 830 mas and contrast of $\sim 10^{-4}$ relative to the host star make this object an ideal early target to be observed with the NIRCam and MIRI coronagraphs. Figure 1 shows synthetic coronagraphic images calculated using an updated version (described in greater detail in Carter et al. 2021a) of the Pandeia Coronagraphy Advanced Kit for Extractions, (PanCAKE, Perrin et al. 2018; Girard et al. 2018). PanCAKE is a Python-based package that extends the capabilities of the primary JWST exposure time calculator (ETC) Pandeia (Pontoppidan et al. 2016) to be applicable to the coronagraphic observing modes of JWST.

Figure 1 also highlights the effect of various image post-processing strategies on the significance of the detection of the

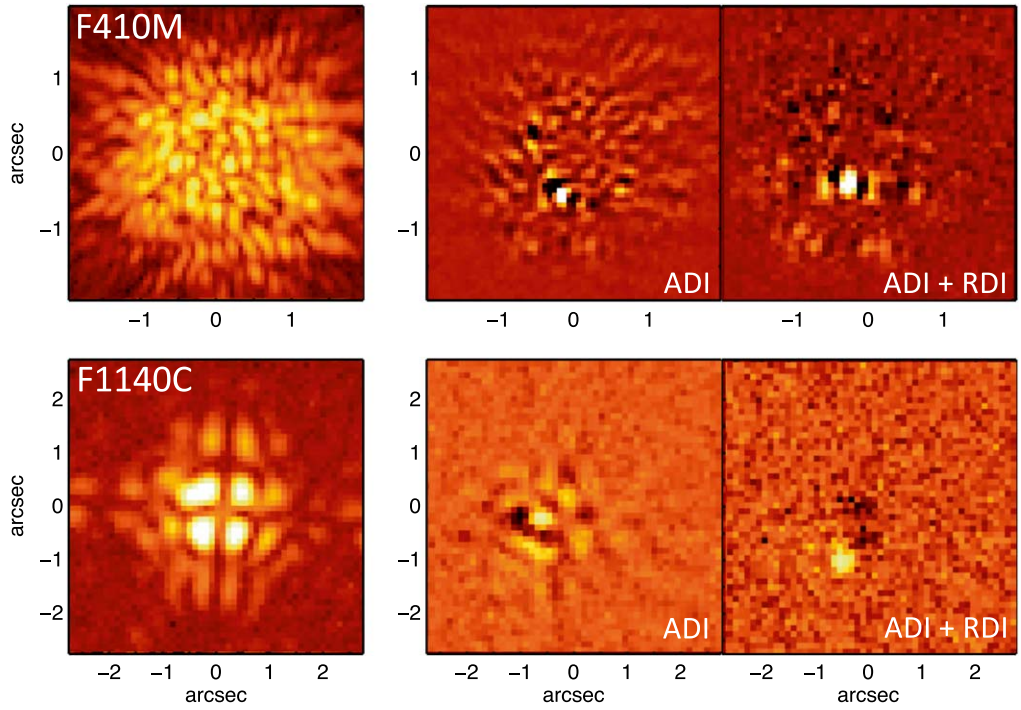

Figure 1. Simulated coronagraphic images of the directly imaged exoplanet HIP 65426b (Chauvin et al. 2017) in the 4.1 μm NIRCam filter (*F410M,* top row), and the 11.4 μm MIRI filter (*F1140C, bottom row*) using the simulation methods described in Carter et al. (2021a). In each set of figures, the left image shows the coronagraphic point-spread function for each bandpass, while the middle and right panels show subsequent image post-processing employing Angular Differential Imaging (ADI) or a combination of ADI with Reference Differential Imaging (labeled "ADI+RDI") that utilizes a small library of images obtained using the small-grid dither strategy (Lajoie et al. 2016).

underlying planet HIP 65426b. The central panels of Figure 1 show the detection using a simple framework based on ADI, taking advantage of the fact that HIP 65426 will be observed in two configurations separated by a physical "roll" of the observatory of a few degrees. This well-tested methodology is based on the heritage of "roll deconvolution" methods developed for HST (Krist et al. 2012; Schneider et al. 2014). Figure 1 also shows the improvement in contrast that can be gained by tapping into a larger pool of PSF reference images to perform Reference Differential Imaging ("RDI," Soummer et al. 2011; Ruane et al. 2019; Sanghi et al. 2022), and labeled "ADI+RDI" in the figure. This method takes advantage of the "small-grid dither" strategy in which repeated observations of a calibration star are obtained at six or nine positions separated by sub-pixel spacings, with the goal of more broadly sampling PSF variations due to varying placement behind the coronagraphic masks.

Numerous studies have demonstrated the improved coronagraphic suppression at small inner working angles by tapping into a much larger "library" of reference images (e.g., Soummer et al. 2011, 2014; Choquet et al. 2016; Ruane et al. 2019; Wahhaj et al. 2021; Sanghi et al. 2022). This potential improvement in inner working angle is even more crucial for JWST which typically has an angular resolution of $\sim$100–140 mas at 3–4 μm, compared to the $\sim$30–50 mas resolution of 8–10 m ground-based telescopes in the near-infrared. This improvement is most pronounced with coronagraphic data sets that (a) have a large number of PSF reference images; and (b) are highly stable in time, such as is expected to be the case for JWST. Indeed, the pool of reference images will inevitably grow over the lifetime of JWST, and our ability to suppress starlight at small inner working angles will improve over time as our library of reference images grows. Thus, it is of paramount importance to determine the correct observing strategy early in the mission, so that the community may tap into the most uniform pool of reference images possible. The coronagraphic data sets obtained as part of this ERS program will mark the first step in this process.

Figure 2 (top panel) shows the planned photometric coverage for the coronagraphic observations of HIP 65426b. As listed in Table 2, the total wavelength coverage for this portion of the program spans from 2.50 μm to 15.5 μm using the NIRCam "MASK335R" (335 round coronagraphic mask) F250M, F300M, F410M, F356W, and F444W filters, as well as the F1140C and F1550C MIRI filters coupled to the FQPM. The transmission profiles of each filter are shown in the top panel of Figure 2, and the horizontal error bars on each point indicate the filter widths (in μm). The continuous curve in the

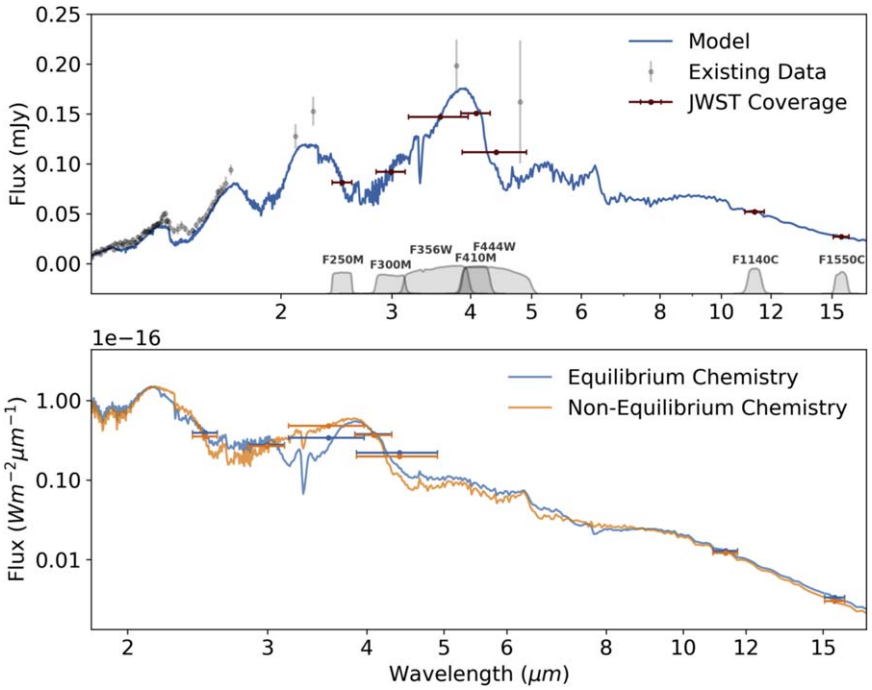

Figure 2. *Top panel:* The spectral coverage of HIP 65426b we will achieve using NIRCam and MIRI Coronagraphy (red points), compared to the existing VLT-SPHERE and NACO photometric points (Cheetham et al. 2019) shown in black/gray, and overlaid with a model ($T_{\rm eff} = 1340$ K, $\log(g) = 3.95$) computed using the tools described in Tremblin et al. (2015). The simulated JWST data points reflect the integral of the flux density over the filter bandpass, divided by the width of the bandpass. *Bottom panel:* Two example synthetic atmosphere models (assuming the same physical parameters for each model) taken from Phillips et al. (2020) illustrating the effects of non-equilibrium chemistry (orange curve) compared to equilibrium chemistry (blue). Also shown are the photometric points from NIRCam and MIRI we will obtain, which will easily have the precision to differentiate between the two models, particularly at 3.56 μm.

top panel of Figure 2 shows a model for a $T_{\rm eff} = 1340$ K and $\log(g) = 3.95$ object, and is based on the results presented in Cheetham et al. (2019). The photometric points in the figure were calculated by integrating the model over the bandpass of each of the filters.

The bottom panel of Figure 2 shows the power of the longer wavelength data that will be available in this ERS program to characterize the atmospheres of substellar objects. The figure shows two synthetic atmospheric models taken from Phillips et al. (2020) which present a set of theoretical atmosphere and evolutionary models for very cool brown dwarfs and self-luminous giant exoplanets generated using the one-dimensional radiative-convective equilibrium code ATMO (Tremblin et al. 2016). The figure shows an atmosphere model based on equilibrium atmospheric chemistry (blue curve), as well as a model characterized by disequilibrium chemistry (orange curve). Evidence for exoplanet atmospheres characterized by disequilibrium chemistry already exist (e.g., Skemer et al. 2012; Konopacky et al. 2013; Miles et al. 2020), and atmospheres can be driven out of equilibrium due to processes that happen on timescales faster than the net chemical reaction timescales that would bring the atmosphere back to equilibrium (e.g., rapid vertical atmospheric mixing driven by gravity waves or convective overshooting; Freytag et al. 1996; Kupka et al. 2018). The models plotted rely on the values of 1618K and $\log(g) = 3.78$ for the HIP 65426b system from (Cheetham et al. 2019) which derived these best-fit parameters using a combination of 1–2.2 μm spectroscopy and photometry from VLT-SPHERE, as well as L' and M' photometry from VLT-NACO. When only considering the band-averaged brightnesses, the two models are virtually identical at 2.50 μm, but are very clearly differentiated at 3.56 μm. Of course, other atmospheric properties besides the presence of disequilibrium chemistry can affect the flux near 3.56 μm. For example, a higher effective temperature ($T_{\rm eff}$) or a lower overall atmospheric metallicity leading to decreased CH_4 would change the strength of the 3.56 μm feature. However, these degeneracies can be broken via other parameters accessed by our data sets, e.g., constraints on the effective temperature afforded by the long-wavelength coverage, and constraints on the atmospheric metallicity from host star abundance measurements. Thus, the very high expected photometric precision of NIRCam, combined with long-wavelength coverage and host star abundance constraints means that our data will be sensitive to the effects of disequilibrium chemistry, which has the largest impact near 3.56 μm given the broad CH_4 feature.

The significant photometric uncertainties indicated by the error bars on the existing ground-based data shown in Figure 2

(top panel) highlight that it is challenging for these data to provide precise constraints on the theoretical atmospheric models of HIP65426b. However, the vastly higher precision NIRCam and MIRI photometry beyond $\sim$2 μm, will allow much tighter constraints on the allowable atmospheric parameters. Along with the vastly increased photometric precision, the longer wavelength coverage provided by our observations will provide a much greater source of leverage for performing an atmospheric retrieval analysis, similar to that described in Section 3.2.1. Specifically, we will carry out forward model fitting to extract the best-fit model parameters reflecting the atmospheric compositions as well as a retrieval analysis to gather constraints on molecular abundances (e.g., CO, H_2O, CH_4), disequilibrium chemistry, and the presents of clouds. With high precision NIRCam and MIRI data beyond $\sim$2 μm, particularly out to $\sim$15 μm on the tail of the SED, our data set will also provide a much better constraint on the broadband emission of HIP65426b.

To demonstrate the sensitivity of coronagraphic observations using both NIRCam and MIRI, Figure 3 shows the expected achievable contrast corresponding to the various stages of image post-processing at 4.1 μm and 11.4 μm shown in Figure 1. The contrast curves were calculated using a modified version of PanCAKE described in Carter et al. (2021a) for the F410M and F1140C filters that we will utilize in this program. Rather than the 5σ contrast curves used historically (e.g., Hinkley et al. 2007), the curves are based on a 3×10^{-7} false positive fraction, taking into account the statistical correction due to small angular separations (Mawet et al. 2014). The contrast curves presented in Figure 3 are also calibrated for the two-dimensional throughput of the coronagraphs as well as the inherent throughput of the Karhunen-Loève Image Projection subtraction routine ("KLIP," Soummer et al. 2012) which uses a principal component analysis approach to build a synthetic reference image for each science image from a library of reference images. Importantly, these contrast curves also take into account dynamical changes in the wavefront error due to the varying thermal state of the optical telescope element (OTE) due to telescope slews, small variations in the tension of the physical structure of the telescope, or vibrations within the OTE (e.g., due to the OTE stray light baffle/insulation closeouts). For each wavelength, Figure 3 displays a curve assuming only a simple roll subtraction (termed "ADI"). Further, Figure 3 also shows the improvement in contrast by a factor of a $\sim$few to ten that can be gained by taking advantage of the small-grid dither strategy (labeled "ADI+RDI" in the figure). As a calibration strategy for our observations of HIP 65426b, we will observe the B2IV star HIP 68245, which is close to the sky to HIP 65426, but has $\sim$8 times the brightness in the mid-infrared (K = 4.49 versus K = 6.77 for HIP 65426). The enhanced brightness of HIP68245 allows us to obtain a nine-point dithered observation of this calibrator without a prohibitively large amount of observing time. Table 2 shows that this calibrator star will be observed in roughly half the charged time as our observations of HIP 65426 (6.0 hr versus 10.4 hr), but with nine times the data volume, enhancing the overall calibration process.

To calculate a representative estimation of the sensitivity to low-mass companions (in Jupiter masses) as a function of projected orbital separation (in au) of these observations, the lower panels of Figure 3 also show the corresponding two-dimensional detection probability maps based on the synthetic contrast curves. These detection probability maps, calculated using the Exoplanet Detection Map Calculator ("Exo-DMC," Bonavita 2020), effectively demonstrate the degree of "completeness" to planetary-mass companions as a function of mass and semimajor axis for a given coronagraphic observation. For a given planet mass and semimajor axis, Exo-DMC simulates an ensemble of orbital geometries with varying planetary eccentricity and inclination to determine which fraction of those realizations, identified by the various completeness contours, would be detected based on the supplied single contrast curve, thus providing a measure of the completeness of the observations. This calculation uses the evolutionary models of Phillips et al. (2020) assuming an age of 14 Myr to convert from the contrast to a physical mass, and so these plots are dependent on the underlying evolutionary models as well the formulation of atmospheric process that they employ.

3.2. *Spectroscopy of a Planetary Mass Companion*

VHS 1256b (Gauza et al. 2015; Miles et al. 2018) is a wide separation ($\sim$103 au), substellar companion ($19 \pm 5\,M_{\rm Jup}$) to a young M7.5 binary star (Stone et al. 2016; Rich et al. 2016). While the VHS 1256 system is not a member of any known kinematic young moving groups, (Gauza et al. 2015) derive an age of 150–300 Myr, consistent with its low surface gravity. With a spectral type of L7, infrared parallax measurements (Dupuy et al. 2020) show that VHS 1256b shares a region in a color–magnitude diagram with other planetary-mass companions that are near the L/T transition, and close to the deuterium burning limit such as HR 8799b, HD 203030B, and 2MASS J22362452 + 4751425b (Marois et al. 2008; Metchev & Hillenbrand 2006; Bowler et al. 2017).

As shown in Table 2, we will observe VHS 1256b using the NIRSpec IFS from 1.66 to 5.27 μm with the G140H, G235H, G395H gratings ($\lambda/\Delta\lambda \sim$ 1500–3500). Our selected exposure time provides a signal-to-noise ratio (SNR) of >20 across the majority of the wavelength range with many features detectable to an SNR of >100. However, these estimations are based on initial simulations, and the actual data may indeed have different SNR values. To probe silicate cloud features at 8 to 12 μm for the first time ever for low surface gravity objects, we will also perform mid-infrared spectroscopy on VHS 1256b from $\sim$5 to 28 μm using the MIRI MRS in all four channels with all three dispersers. To improve the sensitivity of the

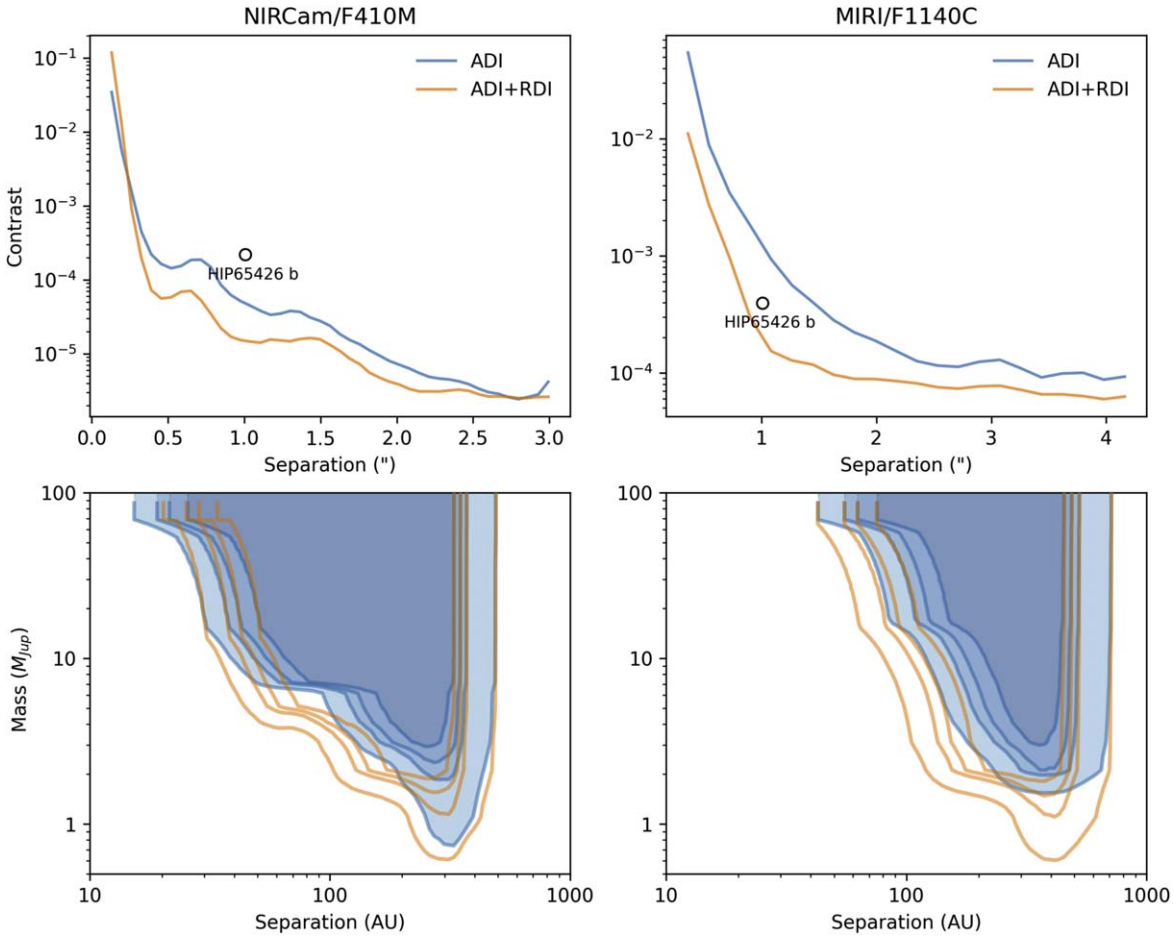

Figure 3. *Top row:* Simulated contrast curves using the updated version of the PanCAKE tool (Carter et al. 2021a) showing the predicted contrast performance in the NIRCam F410M (4.1 μm) and MIRI F1140C (11.4 μm) JWST filters. The two sets of curves illustrate the coronagraphic performance using PSF subtraction based both on Angular Differential Imaging (ADI) as well as a combination of ADI and Reference Differential Imaging (RDI), corresponding to the images shown in Figure 1. The theoretical contrast of the HIP 65426b exoplanet is shown by the circular point. *Bottom row:* The corresponding detection probability maps (Bonavita 2020) based on these contrast curves with the 3%, 60%, 70%, and 80% detection probability contours highlighted.

observations and minimize detector effects, we will utilize four dither positions for both the NIRSpec and MIRI observations.

Historically, the main obstacle to obtaining unbiased spectroscopy of planetary-mass companions from ground-based spectrographs coupled to AO systems has been contamination from uncontrolled, residual scattered starlight within $\sim$1″–2″ (Marois et al. 2006; Hinkley et al. 2007; Pueyo 2016). The relatively large angular separation ($\sim$8″) of VHS 1256b from its host binary pair means that our JWST observations should have minimal contamination of residual scattered starlight. Thus, JWST Spectroscopy of this object will allow high-fidelity detections of molecules from $\sim$2 to 28 μm that will be vital for the understanding of cloud physics driven by dust or thermo-chemical instability under low gravity conditions, as well as searching for evidence of silicate clouds at 8–12 μm. The VHS 1256b spectroscopy should also serve as a valuable community data set for testing spectral extraction algorithms for NIRSpec and MIRI.

Figure 4 shows an example of the signal-to-noise and wavelength coverage for the spectroscopy of the VHS 1256b companion that will be obtained with our program. The figure shows a theoretical model atmosphere of a substellar object with the currently best-fit derived effective temperature and gravity parameters for VHS 1256b (Zhou et al. 2020). To calculate the effective uncertainty in the model as a function of wavelength, this model was then used as input into the JWST ETC, which in turn provides a measure of the expected signal-to-noise as a function of wavelength. Dividing the original model spectrum by this signal-to-noise spectrum effectively provides a measure of the noise as a function of wavelength,

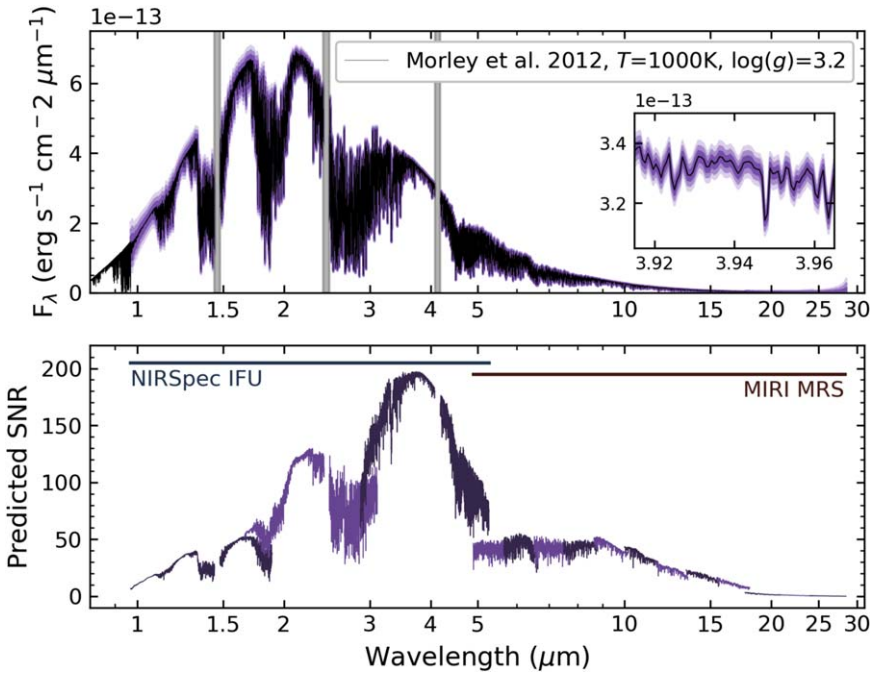

Figure 4. *Top panel:* A synthetic spectrum of the VHS 1256b planetary-mass companion we will obtain using NIRSpec and MIRI, reflecting the actual spectral resolution, as well as a subset of the spectral range that will be covered (inset). The purple regions signify the 1, 2, 3σ confidence intervals in the spectrum, while the gray regions indicate portions of the spectrum where no data will be gathered due to detector gaps. The input model spectrum is based on a synthetic model described in Morley et al. (2012), which has been used in conjunction with the estimated signal-to-noise ratio defined in the ETC, to determine the confidence intervals shown in the plot. *Bottom Panel:* The predicted SNR for the VHS 1256b spectrum, as determined from the JWST ETC.

and this noise is represented by the purple-shaded regions in the figure. The lower panel of Figure 4 shows the SNR as a function of wavelength calculated using the ETC.

3.2.1. A Suite of Atmospheric Retrievals for VHS 1256b

We will employ an extensive retrieval analysis of the reduced spectroscopic data for VHS 1256b, testing various approaches. Exploring a range of atmospheric chemistry parameters will probe whether the atmosphere is in chemical equilibrium versus disequilibrium (Miles et al. 2020; Mollière et al. 2020). We expect that the quality of our spectra will easily be sensitive enough to fully sample the prominent CO features at ∼2.3 and ∼4.3 μm, as well as numerous H_2O and CH_4 features across the majority of the spectral range. By unlocking the mid-IR we will also be able to robustly explore potential cloud structures (Manjavacas et al. 2021) and cloud species present (Burningham et al. 2021). Due to the extensive variability present on VHS 1256b (Bowler et al. 2020), and as the data will be collected over a period of hours, we will also probe signatures of variability within our retrieval analysis.

To simulate the outcome of using an atmospheric retrieval-based approach, Figure 5 shows a demonstration of a simulated retrieval analysis of VHS 1256b comparing HST WFC3 against simulated JWST NIRSpec spectroscopy. For this, employing a forward model created via TauREx3.1 (Waldmann et al. 2015b, 2015a; Al-Refaie et al. 2021b, 2021a) and FastChem (Kitzmann & Stock 2018), we simulated realistic NIRSpec spectroscopy with SNR ranging from ∼50 to ∼250 generated with the JWST ETC. We also simulated a WFC3 data set with a uniform SNR of 50. We then ran retrievals using these simulated observations and wide uniform priors on all model parameters. Figure 5 highlights the novel power JWST can offer for precisely and accurately constraining crucial model parameters within retrievals. However, the improved precision shown in Figure 5 is probably slightly optimistic as: (1) the retrieval algorithm is retrieving its own model input; (2) these simulations use a simplistic forward model; and (3) we assume perfect data reduction/calibration ignoring any photometric variability during the observations. However, we stress that this dramatic increase in precision is driven primarily by the order of magnitude increase in wavelength coverage and spectral points as well as improved SNR. Nonetheless, Figure 5 gives a qualitative sense of the level of improvement that can be gained with the advent of JWST spectroscopy.

3.2.2. Variability Monitoring of VHS 1256b

Quasiperiodic brightness variability is commonly found in field L and T-type brown dwarfs, with periods from 1.5–30 hr,

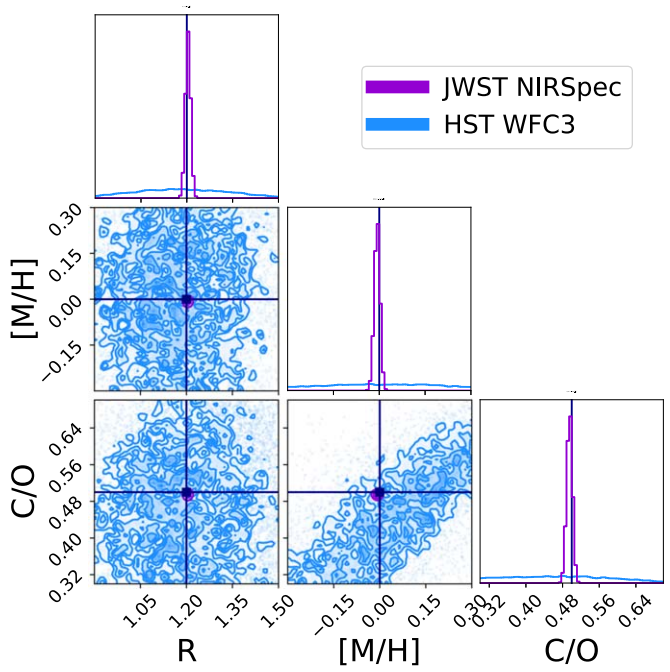

Figure 5. A demonstration of a simulated atmospheric retrieval analysis of VHS 1256b using simulated HST WFC3 and JWST NIRSpec data. The data set for NIRSpec was simulated at an SNR of 50–250 using the JWST ETC, and a uniform SNR = 50 for WFC3. Retrieval analyses were performed to derive the model parameters, demonstrating the power JWST can offer for precisely and accurately constraining crucial model parameters within retrievals.

and amplitudes ranging from 0.01% to 27% (Radigan et al. 2014; Metchev et al. 2015). Young directly imaged exoplanets are likely even more variable, as their free-floating counterparts appear to be particularly variable (Biller et al. 2015a; Apai et al. 2016). VHS 1256b is the most variable of this group; with measured variability amplitudes of >25% over an 8 hr long HST observation (Bowler et al. 2020; Zhou et al. 2020), it may be the most variable substellar object ever observed. Indeed, VHS 1256b is so highly variable that it may vary by up to 10% over our three-hour ERS observation. However, it should be noted that the variability of substellar objects is wavelength dependent (Metchev et al. 2015; Vos et al. 2020), and this has been quantified for VHS 1256b in Zhou et al. (2020). Over ∼1.2 hr on-sky, our program will obtain three consecutive NIRSpec IFS spectra covering 1–5 μm in the following order: 1.66–3.17, 2.37–5.27, and 0.97–1.89 μm. Each spectrum will be taken at four dither positions, providing two temporal samples for each spectral range, separated by ∼12 minutes from the central time point of each spectrum. It is worth noting that we will also record "up-the-ramp" flux measurements, and thus our observations may be sensitive to variability on even shorter timescales. In the extreme case, if VHS 1256b has a similar 1–5 μm variability amplitude in this epoch as in Bowler et al. (2020), this would translate to a ∼few percent change in overall flux across the NIRSpec observation, sufficient to cause non-negligible issues with spectral fitting when stitching together, e.g., the 1.66–3.17 μm spectrum with the 0.97–1.89 μm spectrum (the muted variability in the water bands, however, will facilitate stitching together the spectra). This effect is expected to be even more pronounced with the MIRI MRS observations, which occur over a longer timescale. To address this risk, we have initiated a coordinated ground-based observing campaign that will utilize a suite of longitudinally-distributed observing sites to observe prior to, and ideally in parallel with, the ERS observations. These observations will allow us to correctly stitch together the ERS spectroscopy, and constrain the wavelength-by-wavelength amplitudes and phase shifts.

3.3. Coronagraphy of a Young Circumstellar Disk

HD 141569A is a young circumstellar disk (5 ± 3 Myr, Weinberger et al. 2000) that has been a well-studied target of past space-based (e.g., Augereau et al. 1999a; Weinberger et al. 1999; Konishi et al. 2016) as well as ground-based (Biller et al. 2015b; Perrot et al. 2016; Currie et al. 2016; Bruzzone et al. 2020; Singh et al. 2021) high-contrast imaging efforts. HD 141569A is also a unique system for our understanding of both protoplanetary disk dispersal processes as well as the early stages of debris disk systems. In terms of disk luminosity HD 141569A sits at the transition between protoplanetary and debris disks (Wyatt et al. 2015), and so is a rare object caught in transition between the two phases. Thus, from a purely scientific point of view, our ERS observations will help to illuminate whether e.g., the dust within the disk is primordial or secondary, and how the observed morphological structures relate to planet formation. Our observations of HD 141569A will demonstrate the power JWST holds for characterizing circumstellar debris disks, allowing us to determine the disk's dust size distribution and composition as a function of radius, and search for planet-induced structures in the mid-infrared for the first time.

Given that it is comprised of at least three concentric disk rings, HD 141569A is also an ideal target to test the sensitivity of JWST to extended structures as a function of stellocentric angle, as well as study the effects of various PSF subtraction post-processing algorithms on diffuse structures. We will obtain coronagraphic imaging of HD 141569A from 3.0 to 15.5 μm using both NIRCam and MIRI (Table 2). By utilizing the F300M and F360M NIRCam filters, We will image the disk on and off the 3.0 μm H_2O ice absorption band that is difficult to probe with ground-based telescopes. In addition to using the 10.65 μm and 11.4 μm MIRI filters, we will image the disk at 15.5 μm, one of the primary wavelengths expected to be used for JWST disk imaging going forward. As with the case of the HIP 65426b observations, for a calibration strategy a brighter calibrator star (HD 140986, Table 2) will be used to generate a significant volume of PSF calibration images without a

prohibitively large amount of exposure time. The enhanced brightness of HD 140986 (K =3.64 versus K = 6.82 for HD 141569A) means that we will require 5.4 hr of calibration observations using a five-point dither strategy, compared to 8.1 hr for HD 141569A.

To extract the signal of the disk in the NIRCam data, we will use the KLIP algorithm to subtract the residual scattered starlight using the dithered images of the calibrator star. We will also use recently-developed PSF subtraction algorithms that are known to better preserve the absolute flux of bright extended structures than PCA-based methods, such as the Non-negative Matrix Factorization (Ren et al. 2018) and Data Imputation (Ren et al. 2020), and present a comparison of the results obtained with the different algorithms. The brightness ratio of the disk between the F300M and F360M filters will allow us to constrain the composition of the dust, in particular the ice fraction in the different belts of the system. This will reveal whether the dust is cometary or asteroid-like in nature, and will provide direct observations of how water is radially distributed in the outer parts ($\gtrsim$50 au) of this young system. For this analysis, we will use both a forward modeling approach as well as an empirical approach to measure the surface brightnesses and scattering phase functions in both filters. In both cases, we will compare the data to models created with the MCFOST radiative transfer code (Pinte et al. 2006) which can simulate dust belts with various chemical compositions and grain size distributions.

In the mid-infrared, where the existing resolved images of the HD 141569A disk are from ground-based instruments and only sensitive to the warm inner disk at ∼50 au (Moerchen et al. 2010; Thi et al. 2014; Mawet et al. 2017), very little is known about the thermal properties of the outer disk components at ∼200 and ∼400 au. Similarly, the SED of the system is dominated by the emission of the inner disk between ∼8 μm and ∼40 μm (see Mawet et al. 2017), which also prevents any constraints on the thermal properties of the outer belts. Our MIRI imaging will be sensitive for the first time to the mid-IR emission of the outer belts and spatially separate them from the inner belt emission. These independent measurements of each disk component will allow us to disentangle their individual thermal properties. Simulations of the data we will collect with MIRI based on the model from Thi et al. (2014), indicate that the two outer belts should be directly visible in the three MIRI filters, with little contamination from the star, while the innermost belt will be impacted by both the residual host starlight and obscuration from the 4QPM coronagraph. Given this, HD 141569A thus has the added bonus that this target will serve as a good feasibility test for the MIRI coronagraphs to check whether future observations of protoplanetary disks might be limited by the (nearly) unresolved warmer inner ring components.

After removing the residual starlight using the reference star observations, we will use MIRI imaging for three main applications. First, the 10.65 μm image will let us investigate the transition between the scattered-light and thermal regimes in each belt. While the inner disk 10.65 μm image should be largely dominated by thermal emission, scattered light may be significant in the images of the outer disks. We will use both the MIRI F1065C image and the F300M/F360M NIRCam images to disentangle the scattered-light and thermal contributions of each belt. Second, we will use the 10.65 μm and 11.4 μm images to measure the radial distribution of Polycyclic Aromatic Hydrocarbons (PAH). Unresolved Spitzer IRS observations have previously detected PAH in this system (Sloan et al. 2005; Berné et al. 2009), but it is currently unclear if they are distributed uniformly throughout the disk, in only parts of the disk, or in an outflowing halo of small grains. The F1065C and F1140C data sets will be sensitive to the broad PAH emission feature at 11.3 μm, allowing us to constrain the PAH abundances in each ring. Third, we will use the 10.65 μm and 15.5 μm images to measure the continuum thermal emission of each ring individually and construct a temperature map of the whole system. This will allow us to derive the emissivity of the grains and thus the minimum grain size of each ring through radiative transfer modeling. The distribution of small micron-sized dust inferred from these observations will be particularly powerful when coupled with information about the distribution of larger millimeter-sized dust bodies and CO inferred from ALMA observations (e.g., Di Folco et al. 2020). This will give the grain size distribution over a wider range of particle sizes, and allow us to test for models of grain radial transport through interaction with a remnant gas disk (e.g., Takeuchi & Artymowicz 2001).

Finally, in all NIRCam and MIRI images of HD141569A, we will scrutinize the disk morphology to look for direct and indirect evidence of planets. The system shows large cavities that suggest dynamical clearing by planets (e.g., Wyatt 2005; Konishi et al. 2016; Perrot et al. 2016), and asymmetries in the dust density distribution possibly caused by a massive collision between planetesimals (Singh et al. 2021). The longer wavelengths of JWST offer a more favorable contrast regime to probe for the presence of giant planets than existing shorter wavelength observations, as discussed in Section 1.2. The NIRCam F360M and the MIRI F1065C images will be the best suited to look for planets within the gaps of the system, as they offer the best compromise between contrast limits and spatial resolution.

To simulate the HD 141569A NIRCam data, we use the basic physical parameters listed in Table 3. We first generate a model composed of three rings, of respective semimajor axes 0.″8, 1.″8, and 3.″2. Assuming a distance of 110.6 pc (Gaia Collaboration et al. 2018), these values correspond to radii of 88 , 199 , and 354 AU, based on the findings of Konishi et al. (2016), and Mouillet et al. (2001). We simulate a common 56.°9 inclination from a face-on configuration and a common position angle 356.°1, east of north for the three rings

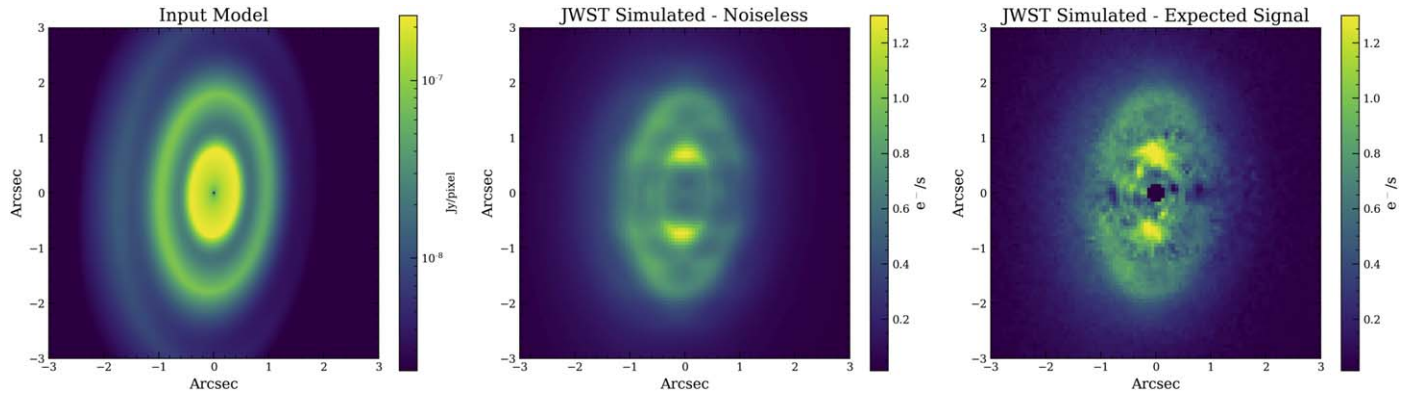

Figure 6. Simulated NIRCam data for our planned observations of HD 141569A using the F300M filter. The left figure shows our input model of the three rings that comprise the HD 141569A disk and described in Table 3, while the middle panel shows a representative NIRCam image free of noise. The right panel shows a simulated image, now including a realistic estimate of the NIRCam noise that we can expect with our ERS observations.

Table 3
Parameters for HD 141569A Model

System Parameters			
Distance (pc)		110.6	
Inclination (°)		56.9	
Position angle (°)		356.1	
Vertical aspect ratio h		0.04	
F300M Stellar flux (Jy)		0.71	
F360M Stellar flux (Jy)		0.50	
Ring Parameters	Ring 1	Ring 2	Ring 3
Semimajor axis ($''$)	0.8	1.8	3.2
Critical radius (au)	88	199	354
Inward density index α_{in}	1.5	5.5	5.5
Outward density index α_{out}	−7.5	−7.5	−3.5
HG parameter g	0.0	0.1	0.3
Peak reflectance ($\times 10^{-4}$ $''^{-2}$)	8.0	2.8	0.4

(Perrot et al. 2016). We use the ring parametric model described in Augereau et al. (1999b) to model the dust density distribution. The radial profile is modeled with an increasing power law (index $\alpha_{\rm in}$) inward of the critical radius quoted above and a decreasing power law (index $\alpha_{\rm out}$) outward from this radius. The power-law indices used to model each of the three rings are displayed in Table 3. The vertical profile of the disks follows a Gaussian profile with a standard deviation increasing radially with an aspect ratio $h = 0.04$ (Thébault 2009).

We simulate the scattering phase function of the rings using a Henyey-Greenstein (HG) in a parametric model with an asymmetry parameter g of 0.0 for the inner ring (Konishi et al. 2016), 0.1 for the middle ring (Weinberger et al. 1999), and 0.3 for the outer ring Clampin et al. (2003). We use optically thin scattered light propagation from the central star, computed with the same code as in Millar-Blanchaer et al. (2015) to simulate synthetic images of the three rings. We then scale the peak surface brightness of each disk to the product between the stellar flux at the considered wavelength and the disk peak reflectance. The left panel of Figure 6 shows this model, free of any detector noise. We obtain the peak reflectance of each ring from previous *HST/NICMOS* data obtained in the F160W filter ($\sim$1.6 μm) from the ALICE archival re-analysis (Hagan et al. 2018), assuming that the dust reflectance is identical at the longer NIRCam wavelengths (gray scattering). We compute the stellar flux in the NIRCam F300M and F360M filters from the JWST online ETC using a Phoenix A1V spectrum scaled to the $K = 6.82$ HD 141569A magnitude (Cutri et al. 2003). The stellar fluxes in the two filters and the peak reflectance of the three rings are reported in Table 3. Figure 6 also shows a simulated image of the data we can expect to receive from our NIRCam imaging of this system, incorporating realistic noise sources.

3.4. Aperture Masking Interferometry

Given its 6.5 m effective aperture, for the purpose of gaining direct images of self-luminous exoplanets, JWST will be ultimately limited by its inner working angle defined by its diffraction limit of $\lambda/D \sim$ 120–140 milliarcseconds at 3–4 μm. For the nearest star-forming regions where the planet formation process is still likely ongoing (e.g., Taurus, $\sim$2 Myr, Kraus et al. 2011) or has recently ceased, (e.g., the Scorpius-Centaurus Association, $\sim$11–16 Myr, de Zeeuw et al. 1999; Preibisch & Mamajek 2008) with characteristic distances of $\sim$140 pc, this angular resolution corresponds to physical separations of 17–20 au, well outside the typical water ice line separations of $\sim$2–3 au where planet formation is thought to be most efficient (Frelikh et al. 2019; Fernandes et al. 2019; Fulton et al. 2021). By dividing the full JWST pupil into a set of smaller sub-apertures, the technique of Aperture Masking

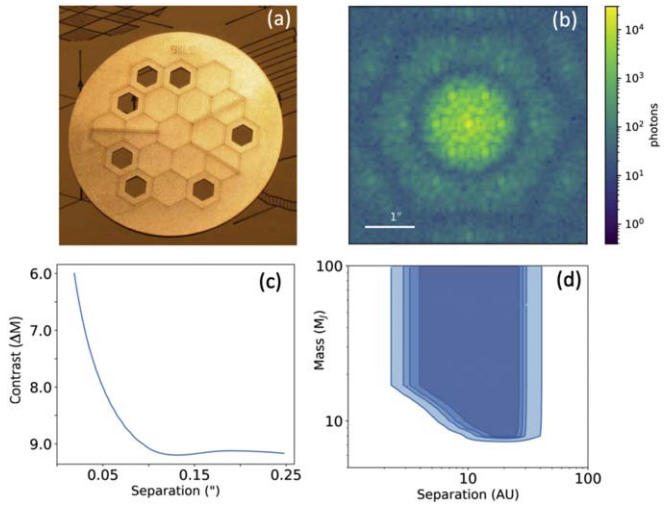

Figure 7. *(a):* An image of the sparse aperture mask installed within the NIRISS instrument (Sivaramakrishnan et al. 2010) for the purpose of performing Aperture Masking Interferometry (Artigau et al. 2014; Greenbaum et al. 2014; Sallum & Skemer 2019). *(b):* A simulated NIRISS interferogram in the F380M filter for an integration time of ∼1.28 s. *(c):* A simulated contrast curve calculated using the methods described in (Sallum & Skemer 2019), and *(d)* the corresponding detection probability map showing the 30, 60, 70 and 80% detection probability contours.

Interferometry ("AMI," Tuthill et al. 2000; Ireland 2013; Sallum & Skemer 2019) can provide modest sensitivity inside the diffraction limit of JWST. This technique has been used extensively from the ground (e.g., Hinkley et al. 2011a; Kraus & Ireland 2012; Hinkley et al. 2015b; Sallum et al. 2015), but never in space, and so obtaining a representative data set as early as possible is critical for future planning. The NIRISS instrument is equipped with a sparse aperture mask (Sivaramakrishnan et al. 2010) containing seven holes, providing 21 distinct "non-redundant" baselines that can be used with the medium-band NIRISS filters from 3.8–4.8 μm (F380M, F430M, and F480M). Figure 7 shows an image of the seven-hole mask, as well as a simulation of the resulting interferogram on the detector using the NIRISS F380M filter generated using the methodology described in Sallum & Skemer 2019, assuming a point source for a total integration time of 1.28 s. With the goal of identifying the limiting systematics inherent in AMI observations we will obtain 3.8 μm sparse aperture masking observations of the HIP 65426 system. Past studies have demonstrated that systems with already-identified wide separation planets may also have additional planets at smaller angular separations (Marois et al. 2010; Wagner et al. 2019; Lagrange et al. 2020; Nowak et al. 2020), and this effort will place constraints on any additional companions in this system. Our proposed observations of the HIP 65426 system are predicted to reach a contrast ranging from 6 to ∼9 mag within the 120 mas JWST diffraction limit at 3.8 μm, providing sensitivity to substellar companions within ∼14 au for this system (Figure 7, lower panels).

4. Analysis Plan & Science Enabling Products for the Broader Community

Our consortium is comprised of a set of four working subgroups, corresponding to: (1) exoplanet coronagraphic imaging with NIRCam and MIRI; (2) debris disk imaging with the same two instruments; (3) spectroscopy of substellar companions with NIRSpec and MIRI; and (4) NIRISS aperture masking interferometry.

Our team will be responsible for delivering a set of SEPs described in more detail below that will be widely available, and will assist the community in preparing future JWST proposals. A final working group will have the task of ensuring the quality of the SEPs. This working group will validate the utility of our internal SEPs for preparing future proposals and provide immediate feedback to the individual working groups regarding the quality of the SEPs.

4.1. Science–Enabling Products

In this section we describe in detail each of the SEPs our consortium will deliver:

Coronagraphic imaging simulator: We will widely distribute an update (Carter et al. 2021a) to the JWST simulation tool PanCAKE (Perrin et al. 2018; Girard et al. 2018) that is an adaptation of the JWST ETC *Pandeia*. This tool will model the impact on coronagraphic imaging due to details of the observatory such as target acquisition offsets, the time evolution of the incoming stellar wavefront, spacecraft rolls, and small-grid dithers. This tool will also preserve all the capabilities of the *Pandeia* simulator for generating coronagraphic scenes with MIRI and NIRCam, but with added accessibility and functionality.

High-Contrast Imaging Analysis Pipeline: We will release a publicly available Python-based high-contrast imaging pipeline to process JWST NIRCam and MIRI coronagraphic imaging data and generate contrast curves based on the existing PyKLIP pipeline (Wang et al. 2015), a Python adaption of the commonly used KLIP algorithm that implements several sophisticated state-of-the-art methods for PSF subtraction and forward modeling of systematics. We will test our pipeline against other leading high-contrast pipelines to ensure consistent results. An online manual will describe the algorithm and provide a tutorial to run the pipeline using the ERS HIP 65426 data. This pipeline will be optimized for detecting point sources, but will also produce scientifically usable images of resolved structures, which we will test and document using the HD 141569A images. By the Cycle 2 proposal deadline, users will be able to simulate realistic scenes with the modified version of PanCAKE that will be provided, which can then be interfaced with PyKLIP to produce realistic simulated reductions. The pipeline will also enable an immediate analysis of data from future JWST cycles.

Contrast Curves: We will use our coronagraphic NIRCam/MIRI imaging and NIRISS aperture masking data of HIP

65426 to provide contrast curves showing the point-source sensitivity of JWST as a function of wavelength and stellocentric angle. To reflect various post-processing strategies, we will provide multiple curves per bandpass of contrast (in units of delta-magnitude) versus angular separation.

Aperture Masking Analysis Pipeline: We will release a publicly available Python-based pipeline to process simulated NIRISS AMI data generating a contrast curve and detection tests for single point-source companions. This will be in place prior to the Cycle 2 proposal deadline along with an online tutorial to guide users to reproduce our team's results. The pipeline will enable rapid sensitivity estimates for proposers in future cycles, as well as fast analysis of future data sets.

Communication of Best Practices: The wide variety of JWST's high-contrast modes will spawn numerous technical questions about best practices for observations and data post-processing. For example, the best strategy for utilizing JWST in its coronagraphic mode for various point-source science cases is a priori not obvious. This same question has been an active area of research in the high-contrast imaging community for the past decade, even for ground-based efforts (e.g., Xuan et al. 2018; Wahhaj et al. 2021). For JWST, there is an expectation that RDI will be more effective than ADI due to its limited ability to achieve large roll angles, but it is a clear goal of this program to establish the point in an observation sequence where one method becomes beneficial relative to another. While our ERS program is not intended to be comprehensive, we will make clear recommendations to future JWST proposers about the following:

1. For what observing scenarios does RDI become more effective than ADI? We will also establish whether this crossover point depends on the variety of PSF subtraction, e.g., the Locally Optimized Combination of Images versus KLIP (Lafrenière et al. 2007; Soummer et al. 2012).
2. At what angular separations does AMI achieve contrast that is superior to coronagraphic imaging?
3. To what extent do small-grid dithers for PSF reference stars improve the final contrasts?

5. Summary & Conclusions

The ERS program described in this work will utilize all four JWST instruments to carry out some of the first direct characterizations of planetary-mass companions at wavelengths beyond $\sim$5 μm, as well as image a circumstellar disk in the mid-infrared with unprecedented sensitivity. Specifically, our program will carry out:

1. Coronagraphy of an Extrasolar Planet: Our program will gather photometric measurements of an extrasolar planet with unprecedented sensitivity from 3–5 μm, as well as gather the first-ever coronagraphic observations beyond 5 μm. Our team will produce tools to aid the community in preparing future JWST proposals such as an update to the JWST coronagraphic imaging simulator PanCAKE, a standalone high-contrast imaging analysis pipeline, as well as contrast curves that define the coronagraphic performance of JWST.
2. Spectroscopy of a planetary-mass companion: We will obtain spectroscopy beyond 20 μm of the planetary-mass companion VHS 1256b. This data set will represent an accurate performance of the spectroscopic capabilities of JWST using NIRSpec and MIRI, and will be a valuable resource for the community to prepare proposals related to spectroscopy going forward.
3. Coronagraphy of a circumstellar disk: We will obtain corongraphy out to 15.5 μm of HD 141569A, a young circumstellar disk, providing an understanding of JWST's sensitivity to extended structures as a function of stellocentric angle, and sampling the disk brightness on and off the 3.0 μm H_2O ice feature.
4. Aperture Masking Interferometry: To evaluate the sensitivity of JWST near its fundamental diffraction limit of $\lambda/D \sim 120$–140 milliarcseconds at wavelengths of 3-4 μm, we will carry out observations of the HIP 65426 system. These observations will have sensitivity to substellar companions in this system within $\sim$14 au, as well as identify the limiting systematics inherent in AMI observations.

We have assembled a broad and representative consortium that comprises a large fraction of the entire high-contrast imaging community. Our team members range from senior experts with decades of experience in exoplanet and disk imaging with HST, infrared astronomy (e.g., Spitzer) and adaptive optics, to early career researchers advancing the state-of-the-art in high-contrast image processing and exoplanet atmosphere modeling. Through a series of calls and open consortium in-person meetings, we have drawn inclusively on a wide range of perspectives in identifying the highest priority investigations needed prior to Cycle 2. In addition to the scientific outcomes highlighted in this work, our program will also (critically) assess the performance of the observatory in the key modes expected to be commonly used for exoplanet direct imaging and spectroscopy, optimize data calibration and processing, and generate representative data sets that will enable a broad user base to effectively plan for general observing programs in future cycles. While this ERS program directly addresses the direct imaging of young, Jovian-mass planets with JWST, this effort marks an important milestone in the long-term effort to image much lower mass, terrestrial planets with future large-scale space missions.

We thank the anonymous referee for numerous helpful suggestions, which significantly improved the manuscript. S. H. acknowledges the significant harm caused to members

of the LGBTQIA+ community in the Department of State and NASA, while under the leadership of James Webb as Under Secretary of State and NASA Administrator, respectively. This project was supported by a grant from STScI (JWST-ERS-01386) under NASA contract NAS5-03127. M.T.is supported by JSPS KAKENHI Grant No.18H05442. M.B. acknowledges support from the Deutsche Forschungsgemeinschaft (DFG) through grant Kr 2164/13–2. K.W. acknowledges support from NASA through the NASA Hubble Fellowship grant HST-HF2-51472.001-A awarded by the Space Telescope Science Institute, which is operated by the Association of Universities for Research in Astronomy, Incorporated, under NASA contract NAS5-26555.

ORCID iDs

Sasha Hinkley https://orcid.org/0000-0001-8074-2562
Aarynn L. Carter https://orcid.org/0000-0001-5365-4815
Shrishmoy Ray https://orcid.org/0000-0003-2259-3911
Maxwell A. Millar-Blanchaer https://orcid.org/0000-0001-6205-9233
Polychronis Patapis https://orcid.org/0000-0001-8718-3732
Marshall Perrin https://orcid.org/0000-0002-3191-8151
Karl Stapelfeldt https://orcid.org/0000-0002-2805-7338
Jason Wang, https://orcid.org/0000-0003-0774-6502
Kimberly Ward-Duong, https://orcid.org/0000-0002-4479-8291
Anthony Boccaletti https://orcid.org/0000-0001-9353-2724
Julien H. Girard https://orcid.org/0000-0001-8627-0404
Paul Kalas https://orcid.org/0000-0002-6221-5360
Jens Kammerer https://orcid.org/0000-0003-2769-0438
Pierre Kervella https://orcid.org/0000-0003-0626-1749
Jarron Leisenring https://orcid.org/0000-0002-0834-6140
Yifan Zhou https://orcid.org/0000-0003-2969-6040
Michael Meyer https://orcid.org/0000-0003-2232-7664
Michael C. Liu https://orcid.org/0000-0003-0241-8956
Olivier Absil https://orcid.org/0000-0002-4006-6237
Mariangela Bonavita https://orcid.org/0000-0002-7520-8389
Mark Booth https://orcid.org/0000-0001-8568-6336
Christine Chen https://orcid.org/0000-0002-8382-0447
Camilla Danielski, https://orcid.org/0000-0002-3729-2663
Matthew De Furio https://orcid.org/0000-0003-1863-4960
Samuel M. Factor https://orcid.org/0000-0002-8332-8516
Jonathan J. Fortney https://orcid.org/0000-0002-9843-4354
Alexandra Greenbaum https://orcid.org/0000-0002-7162-8036
Markus Janson https://orcid.org/0000-0001-8345-593X
Matthew Kenworthy https://orcid.org/0000-0002-7064-8270
Masayuki Kuzuhara, https://orcid.org/0000-0002-4677-9182
Raquel Martinez https://orcid.org/0000-0001-6301-896X
Christian Marois, https://orcid.org/0000-0002-4164-4182
Brenda Matthews, https://orcid.org/0000-0003-3017-9577
Elisabeth C. Matthews https://orcid.org/0000-0003-0593-1560
Sascha P. Quanz https://orcid.org/0000-0003-3829-7412
Isabel Rebollido https://orcid.org/0000-0002-4388-6417
Emily Rickman https://orcid.org/0000-0003-4203-9715
Matthias Samland https://orcid.org/0000-0001-9992-4067
B. Sargent, https://orcid.org/0000-0001-9855-8261
Anand Sivaramakrishnan https://orcid.org/0000-0003-1251-4124
Jordan M. Stone https://orcid.org/0000-0003-0454-3718
Motohide Tamura,, https://orcid.org/0000-0002-6510-0681
Arthur Vigan https://orcid.org/0000-0002-5902-7828

References

Al-Refaie, A. F., Changeat, Q., Venot, O., et al. 2021a, ApJ, 932, 123
Al-Refaie, A. F., Changeat, Q., Waldmann, I. P., & Tinetti, G. 2021b, ApJ, 917, 37
Amara, A., & Quanz, S. P. 2012, MNRAS, 427, 948
Apai, D., Kasper, M., Skemer, A., et al. 2016, ApJ, 820, 40
Artigau, É., Sivaramakrishnan, A., Greenbaum, A. Z., et al. 2014, Proc. SPIE, 9143, 914340
Augereau, J. C., Lagrange, A. M., Mouillet, D., & Ménard, F. 1999a, A&A, 350, L51
Augereau, J. C., Lagrange, A. M., Mouillet, D., et al. 1999b, A&A, 348, 557
Avenhaus, H., Quanz, S. P., Garufi, A., et al. 2018, ApJ, 863, 44
Bagnasco, G., Kolm, M., Ferruit, P., et al. 2007, Proc. SPIE, 6692, 66920M
Barman, T. S., Konopacky, Q. M., Macintosh, B., & Marois, C. 2015, ApJ, 804, 61
Barman, T. S., Macintosh, B., Konopacky, Q. M., & Marois, C. 2011, ApJ, 733, 65
Baudoz, P., Boccaletti, A., Riaud, P., et al. 2006, PASP, 118, 765
Beichman, C. A., Rieke, M., Eisenstein, D., et al. 2012, Proc. SPIE, 8442, 84422N
Beichman, C. A., Krist, J., Trauger, J. T., et al. 2010, PASP, 122, 162
Berné, O., Joblin, C., Fuente, A., & Ménard, F. 2009, A&A, 495, 827
Beuzit, J. L., Vigan, A., Mouillet, D., et al. 2019, A&A, 631, A155
Biller, B. A., Vos, J., Bonavita, M., et al. 2015a, ApJL, 813, L23
Biller, B. A., Liu, M. C., Rice, K., et al. 2015b, MNRAS, 450, 4446
Birkmann, S. M., Ferruit, P., Giardino, G., et al. 2022, A&A, 661, A83
Boccaletti, A., Baudoz, P., Baudrand, J., et al. 2005, AdSpR, 36, 1099
Boccaletti, A., Lagage, P. O., Baudoz, P., et al. 2015, PASP, 127, 633
Bohn, A. J., Kenworthy, M. A., Ginski, C., et al. 2020, ApJL, 898, L16
Bonavita, M. 2020, Exo-DMC: Exoplanet Detection Map Calculator, Astrophysics Source Code Library, record, ascl:2010.008
Bowler, B. P. 2016, PASP, 128, 102001
Bowler, B. P., Liu, M. C., Dupuy, T. J., & Cushing, M. C. 2010, ApJ, 723, 850
Bowler, B. P., Zhou, Y., Morley, C. V., et al. 2020, ApJL, 893, L30
Bowler, B. P., Liu, M. C., Mawet, D., et al. 2017, AJ, 153, 18
Brande, J., Barclay, T., Schlieder, J. E., et al. 2020, AJ, 159, 18
Bruzzone, J. S., Metchev, S., Duchêne, G., et al. 2020, AJ, 159, 53
Burningham, B., Faherty, J. K., Gonzales, E. C., et al. 2021, MNRAS, 506, 1944
Carter, A. L., Skemer, A. J. I., Danielski, C., et al. 2021a, Proc. SPIE, 11823, 118230H
Carter, A. L., Hinkley, S., Bonavita, M., et al. 2021b, MNRAS, 501, 1999
Cassan, A., Kubas, D., Beaulieu, J. P., et al. 2012, Natur, 481, 167
Cavarroc, C., Amiaux, J., Baudoz, P., et al. 2008, Proc. SPIE, 7010, 70100W
Chabrier, G., Baraffe, I., Selsis, F., et al. 2007, in Protostars and Planets V, ed. B. Reipurth, D. Jewitt, & K. Keil (Tucson, AZ: Univ. Arizona Press), 623
Chauvin, G., Lagrange, A., Dumas, C., et al. 2004, A&A, 425, L29
Chauvin, G., Desidera, S., Lagrange, A.-M., et al. 2017, A&A, 605, L9

Cheetham, A. C., Samland, M., Brems, S. S., et al. 2019, A&A, 622, A80
Chiang, E., Kite, E., Kalas, P., et al. 2009, ApJ, 693, 734
Chilcote, J., Konopacky, Q., De Rosa, R. J., et al. 2020, Proc. SPIE, 11447, 114471S
Choquet, É., Perrin, M. D., Chen, C. H., et al. 2016, ApJL, 817, L2
Clampin, M., Krist, J. E., Ardila, D. R., et al. 2003, AJ, 126, 385
Cridland, A. J., Eistrup, C., & van Dishoeck, E. F. 2019, A&A, 627, A127
Cridland, A. J., Pudritz, R. E., & Alessi, M. 2016, MNRAS, 461, 3274
Currie, T., Burrows, A., Itoh, Y., et al. 2011, ApJ, 729, 128
Currie, T., Grady, C. A., Cloutier, R., et al. 2016, ApJL, 819, L26
Currie, T., Brandt, T. D., Uyama, T., et al. 2018, AJ, 156, 291
Cushing, M. C., Roellig, T. L., Marley, M. S., et al. 2006, ApJ, 648, 614
Cutri, R. M., Skrutskie, M. F., van Dyk, S., et al. 2003, 2MASS All Sky Catalog of point sources
De Rosa, R. J., Rameau, J., Patience, J., et al. 2016, ApJ, 824, 121
de Zeeuw, P. T., Hoogerwerf, R., de Bruijne, J. H. J., et al. 1999, AJ, 117, 354
Desidera, S., Chauvin, G., Bonavita, M., et al. 2021, A&A, 651, A70
Di Folco, E., Péricaud, J., Dutrey, A., et al. 2020, A&A, 635, A94
Doyon, R., Hutchings, J. B., Beaulieu, M., et al. 2012, Proc. SPIE, 8442, 84422R
Dressing, C. D., & Charbonneau, D. 2013, ApJ, 767, 95
Dupuy, T. J., Liu, M. C., Magnier, E. A., et al. 2020, RNAAS, 4, 54
Esposito, T. M., Kalas, P., Fitzgerald, M. P., et al. 2020, AJ, 160, 24
Faherty, J. K., Riedel, A. R., Cruz, K. L., et al. 2016, ApJS, 225, 10
Fernandes, R. B., Mulders, G. D., Pascucci, I., et al. 2019, ApJ, 874, 81
Filacchione, G., Ciarniello, M., Capaccioni, F., et al. 2014, Icarus, 241, 45
Forgan, D., & Rice, K. 2013, MNRAS, 432, 3168
Fortney, J. J., Mordasini, C., Nettelmann, N., et al. 2013, ApJ, 775, 80
Frelikh, R., Jang, H., Murray-Clay, R. A., & Petrovich, C. 2019, ApJL, 884, L47
Freytag, B., Ludwig, H. G., & Steffen, M. 1996, A&A, 313, 497
Fulton, B. J., Rosenthal, L. J., Hirsch, L. A., et al. 2021, ApJS, 255, 14
Gaia Collaboration, Brown, A. G. A., Vallenari, A., et al. 2018, A&A, 616, A1
Galicher, R., Marois, C., Macintosh, B., et al. 2011, ApJL, 739, L41
Gardner, J. P., Mather, J. C., Clampin, M., et al. 2006, SSRv, 123, 485
Gauza, B., Béjar, V. J. S., Pérez-Garrido, A., et al. 2015, ApJ, 804, 96
Girard, J. H., Blair, W., Brooks, B., et al. 2018, Proc. SPIE, 10698, 106983V
Gravity Collaboration, Lacour, S., Nowak, M., et al. 2019, A&A, 623, L11
Green, J. J., Beichman, C., Basinger, S. A., et al. 2005, Proc. SPIE, 5905, 185
Greenbaum, A. Z., Pueyo, L., Sivaramakrishnan, A., & Lacour, S. 2014, ApJ, 798, 68
Grillmair, C. J., Charbonneau, D., Burrows, A., et al. 2007, ApJL, 658, L115
Grillmair, C. J., Burrows, A., Charbonneau, D., et al. 2008, Natur, 456, 767
Hagan, J. B., Choquet, É., Soummer, R., & Vigan, A. 2018, AJ, 155, 179
Hinkley, S., Carpenter, J. M., Ireland, M. J., & Kraus, A. L. 2011a, ApJL, 730, L21
Hinkley, S., Oppenheimer, B. R., Zimmerman, N., et al. 2011b, PASP, 123, 74
Hinkley, S., Oppenheimer, B. R., Soummer, R., et al. 2007, ApJ, 654, 633
Hinkley, S., Bowler, B. P., Vigan, A., et al. 2015a, ApJL, 805, L10
Hinkley, S., Kraus, A. L., Ireland, M. J., et al. 2015b, ApJL, 806, L9
Hinkley, S., Matthews, E. C., Lefevre, C., et al. 2021, ApJ, 912, 115
Hubeny, I., & Burrows, A. 2007, ApJ, 669, 1248
Hughes, A. M., Duchêne, G., & Matthews, B. C. 2018, ARA&A, 56, 541
Ireland, M. J. 2013, MNRAS, 433, 1718
Jakobsen, P., Ferruit, P., Alves de Oliveira, C., et al. 2022, A&A, 661, A80
Janson, M., Quanz, S. P., Carson, J. C., et al. 2015, A&A, 574, A120
Janson, M., Gratton, R., Rodet, L., et al. 2021, Natur, 600, 231
Kammerer, J., Lacour, S., Stolker, T., et al. 2021, A&A, 652, A57
Kitzmann, D., & Stock, J. 2018, FastChem: An ultra-fast equilibrium chemistry, Astrophysics Source Code Library, ascl:1804.025
Konishi, M., Grady, C. A., Schneider, G., et al. 2016, ApJL, 818, L23
Konopacky, Q. M., Barman, T. S., Macintosh, B. A., & Marois, C. 2013, Science, 339, 1398
Kratter, K. M., Murray-Clay, R. A., & Youdin, A. N. 2010, ApJ, 710, 1375
Kraus, A. L., & Ireland, M. J. 2012, ApJ, 745, 5
Kraus, A. L., Ireland, M. J., Martinache, F., & Hillenbrand, L. A. 2011, ApJ, 731, 8
Krist, J. E., Stapelfeldt, K. R., Bryden, G., & Plavchan, P. 2012, AJ, 144, 45
Krist, J. E., Beichman, C. A., Trauger, J. T., et al. 2007, Proc. SPIE, 6693, 66930H
Kupka, F., Zaussinger, F., & Montgomery, M. H. 2018, MNRAS, 474, 4660
Lacour, S., Wang, J. J., Rodet, L., et al. 2021, A&A, 654, L2
Lafrenière, D., Marois, C., Doyon, R., & Barman, T. 2009, ApJL, 694, L148
Lafrenière, D., Marois, C., Doyon, R., et al. 2007, ApJ, 660, 770
Lagrange, A., Bonnefoy, M., Chauvin, G., et al. 2010, Science, 329, 57
Lagrange, A. M., Rubini, P., Nowak, M., et al. 2020, A&A, 642, A18
Lajoie, C.-P., Soummer, R., Pueyo, L., et al. 2016, Proc. SPIE, 9904, 99045K
Langlois, M., Gratton, R., Lagrange, A. M., et al. 2021, A&A, 651, A71
Liu, M. C., Dupuy, T. J., & Allers, K. N. 2016, ApJ, 833, 96
Looper, D. L., Kirkpatrick, J. D., Cutri, R. M., et al. 2008, ApJ, 686, 528
Macintosh, B., Graham, J. R., Barman, T., et al. 2015, Science, 350, 64
Macintosh, B., Chilcote, J. K., Bailey, V. P., et al. 2018, Proc. SPIE, 10703, 107030K
Madhusudhan, N., Bitsch, B., Johansen, A., & Eriksson, L. 2017, MNRAS, 469, 4102
Males, J. R., Close, L. M., Miller, K., et al. 2018, Proc. SPIE, 10703, 1070309
Manjavacas, E., Karalidi, T., Vos, J. M., et al. 2021, AJ, 162, 179
Marley, M. S., Saumon, D., Cushing, M., et al. 2012, ApJ, 754, 135
Marois, C., Lafrenière, D., Doyon, R., et al. 2006, ApJ, 641, 556
Marois, C., Macintosh, B., Barman, T., et al. 2008, Science, 322, 1348
Marois, C., Zuckerman, B., Konopacky, Q. M., et al. 2010, Natur, 468, 1080
Matthews, E., Hinkley, S., Vigan, A., et al. 2017, ApJL, 843, L12
Matthews, E., Hinkley, S., Vigan, A., et al. 2018, MNRAS, 480, 2757
Mawet, D., Milli, J., Wahhaj, Z., et al. 2014, ApJ, 792, 97
Mawet, D., Choquet, É., Absil, O., et al. 2017, AJ, 153, 44
Mawet, D., Bond, C. Z., Delorme, J. R., et al. 2018, Proc. SPIE, 10703, 1070306
Metchev, S. A., & Hillenbrand, L. A. 2006, ApJ, 651, 1166
Metchev, S. A., Heinze, A., Apai, D., et al. 2015, ApJ, 799, 154
Miles, B. E., Skemer, A. J., Barman, T. S., et al. 2018, ApJ, 869, 18
Miles, B. E., Skemer, A. J. I., Morley, C. V., et al. 2020, AJ, 160, 63
Millar-Blanchaer, M. A., Graham, J. R., Pueyo, L., et al. 2015, ApJ, 811, 18
Moerchen, M. M., Telesco, C. M., & Packham, C. 2010, ApJ, 723, 1418
Mollière, P., Stolker, T., Lacour, S., et al. 2020, A&A, 640, A131
Mollière, P., Molyarova, T., Bitsch, B., et al. 2022, arXiv:2204.13714
Mordasini, C., van Boekel, R., Mollière, P., et al. 2016, ApJ, 832, 41
Morley, C. V., Fortney, J. J., Marley, M. S., et al. 2012, ApJ, 756, 172
Morley, C. V., Kreidberg, L., Rustamkulov, Z., et al. 2017, ApJ, 850, 121
Morrison, S., & Malhotra, R. 2015, ApJ, 799, 41
Mouillet, D., Lagrange, A. M., Augereau, J. C., & Ménard, F. 2001, A&A, 372, L61
Nielsen, E. L., De Rosa, R. J., Macintosh, B., et al. 2019, AJ, 158, 13
Nowak, M., Lacour, S., Lagrange, A. M., et al. 2020, A&A, 642, L2
Öberg, K. I., Murray-Clay, R., & Bergin, E. A. 2011, ApJL, 743, L16
Otten, G. P. P. L., Vigan, A., Muslimov, E., et al. 2021, A&A, 646, A150
Perrin, M. D., Pueyo, L., Van Gorkom, K., et al. 2018, Proc. SPIE, 10698, 1069809
Perrot, C., Boccaletti, A., Pantin, E., et al. 2016, A&A, 590, L7
Petrus, S., Bonnefoy, M., Chauvin, G., et al. 2021, A&A, 648, A59
Phillips, M. W., Tremblin, P., Baraffe, I., et al. 2020, A&A, 637, A38
Pinte, C., Ménard, F., Duchêne, G., & Bastien, P. 2006, A&A, 459, 797
Poleski, R., Skowron, J., Mróz, P., et al. 2020, AcA, 71, 1
Pollack, J. B., Hubickyj, O., Bodenheimer, P., et al. 1996, Icar, 124, 62
Pontoppidan, K. M., Pickering, T. E., Laidler, V. G., et al. 2016, Proc. SPIE, 9910, 991016
Preibisch, T., & Mamajek, E. 2008, in The Nearest OB Association: Scorpius-Centaurus (Sco OB2), ed. B. Reipurth, 235
Pueyo, L. 2016, ApJ, 824, 117
Quanz, S. P., Absil, O., Benz, W., et al. 2021, Experimental Astronomy
Radigan, J., Lafrenière, D., Jayawardhana, R., & Artigau, E. 2014, ApJ, 793, 75
Rameau, J., Chauvin, G., Lagrange, A.-M., et al. 2013, ApJL, 772, L15
Ren, B., Pueyo, L., Chen, C., et al. 2020, ApJ, 892, 74
Ren, B., Pueyo, L., Zhu, G. B., et al. 2018, ApJ, 852, 104
Rich, E. A., Currie, T., Wisniewski, J. P., et al. 2016, ApJ, 830, 114
Rieke, G. H., Wright, G. S., Böker, T., et al. 2015, PASP, 127, 584
Rieke, M. J., Kelly, D., & Horner, S. 2005, Proc. SPIE, 5904, 1
Rizzuto, A. C., Ireland, M. J., & Robertson, J. G. 2011, MNRAS, 416, 3108
Rouan, D., Riaud, P., Boccaletti, A., et al. 2000, PASP, 112, 1479
Ruane, G., Ngo, H., Mawet, D., et al. 2019, AJ, 157, 118

Sallum, S., & Skemer, A. 2019, JATIS, 5, 018001
Sallum, S., Follette, K. B., Eisner, J. A., et al. 2015, Natur, 527, 342
Sanghi, A., Zhou, Y., & Bowler, B. P. 2022, AJ, 163, 119
Schlieder, J. E., Beichman, C. A., Meyer, M. R., & Greene, T. 2016, in 2016 IAU Symp. 314, Young Stars and Planets Near the Sun, ed. J. H. Kastner, B. Stelzer, & S. A. Metchev (Cambridge: Cambridge Univ. Press), 288
Schneider, G., Gaspar, A., Debes, J., et al. 2017, Enabling Narrow(est) IWA Coronagraphy with STIS BAR5 and BAR10 Occulters, Tech. Rep., STScI, 3
Schneider, G., Grady, C. A., Hines, D. C., et al. 2014, AJ, 148, 59
Sing, D. K., Fortney, J. J., Nikolov, N., et al. 2016, Natur, 529, 59
Singh, G., Bhowmik, T., Boccaletti, A., et al. 2021, A&A, 653, A79
Sivaramakrishnan, A., Lafrenière, D., Tuthill, P. G., et al. 2010, Proc. SPIE, 7731, 77313W
Sivaramakrishnan, A., Lafrenière, D., Ford, K. E. S., et al. 2012, Proc. SPIE, 8442, 84422S
Skemer, A. J., Hinz, P. M., Esposito, S., et al. 2012, ApJ, 753, 14
Skemer, A. J., Marley, M. S., Hinz, P. M., et al. 2014, ApJ, 792, 17
Skemer, A. J., Morley, C. V., Zimmerman, N. T., et al. 2016, ApJ, 817, 166
Sloan, G. C., Keller, L. D., Forrest, W. J., et al. 2005, ApJ, 632, 956
Snellen, I., de Kok, R., Birkby, J. L., et al. 2015, A&A, 576, A59
Sorahana, S., & Yamamura, I. 2012, ApJ, 760, 151
Soulain, A., Sivaramakrishnan, A., Tuthill, P., et al. 2020, Proc. SPIE, 11446, 1144611
Soummer, R., Hagan, J. B., Pueyo, L., et al. 2011, ApJ, 741, 55
Soummer, R., Pueyo, L., & Larkin, J. 2012, ApJL, 755, L28
Soummer, R., Perrin, M. D., Pueyo, L., et al. 2014, ApJL, 786, L23
Stolker, T., Quanz, S. P., Todorov, K. O., et al. 2020, A&A, 635, A182
Stone, J. M., Skemer, A. J., Kratter, K. M., et al. 2016, ApJL, 818, L12
Takeuchi, T., & Artymowicz, P. 2001, ApJ, 557, 990
The LUVOIR Team 2019, arXiv:1912.06219
Thébault, P. 2009, A&A, 505, 1269
Thi, W. F., Pinte, C., Pantin, E., et al. 2014, A&A, 561, A50
Tremblin, P., Amundsen, D. S., Chabrier, G., et al. 2016, ApJL, 817, L19
Tremblin, P., Amundsen, D. S., Mourier, P., et al. 2015, ApJL, 804, L17
Tuthill, P. G., Monnier, J. D., Danchi, W. C., et al. 2000, PASP, 112, 555
Vigan, A., Fontanive, C., Meyer, M., et al. 2021, A&A, 651, A72
Vos, J. M., Allers, K. N., & Biller, B. A. 2017, ApJ, 842, 78
Vos, J. M., Biller, B. A., Allers, K. N., et al. 2020, AJ, 160, 38
Wagner, K., Apai, D., & Kratter, K. M. 2019, ApJ, 877, 46
Wagner, K., Boehle, A., Pathak, P., et al. 2021, NatCo, 12, 922
Wahhaj, Z., Milli, J., Romero, C., et al. 2021, A&A, 648, A26
Waldmann, I. P., Rocchetto, M., Tinetti, G., et al. 2015a, ApJ, 813, 13
Waldmann, I. P., Tinetti, G., Rocchetto, M., et al. 2015b, ApJ, 802, 107
Wang, J. J., Ruffio, J.-B., De Rosa, R. J., et al. 2015, pyKLIP: PSF Subtraction for Exoplanets and Disks, Astrophysics Source Code Library, record, ascl:1506.001
Wang, J. J., Vigan, A., Lacour, S., et al. 2021a, AJ, 161, 148
Wang, J. J., Ruffio, J.-B., Morris, E., et al. 2021b, AJ, 162, 148
Weinberger, A. J., Becklin, E. E., Schneider, G., et al. 1999, ApJL, 525, L53
Weinberger, A. J., Rich, R. M., Becklin, E. E., et al. 2000, ApJ, 544, 937
Wright, G. S., Wright, D., Goodson, G. B., et al. 2015, PASP, 127, 595
Wyatt, M. C. 2003, ApJ, 598, 1321
Wyatt, M. C. 2005, A&A, 440, 937
Wyatt, M. C. 2008, ARA&A, 46, 339
Wyatt, M. C., Panić, O., Kennedy, G. M., & Matrà, L. 2015, Ap&SS, 357, 103
Xuan, W. J., Mawet, D., Ngo, H., et al. 2018, AJ, 156, 156
Zahnle, K., Marley, M. S., Morley, C. V., & Moses, J. I. 2016, ApJ, 824, 137
Zhou, Y., Bowler, B. P., Morley, C. V., et al. 2020, AJ, 160, 77
Zhou, Y., Bowler, B. P., Wagner, K. R., et al. 2021, AJ, 161, 244